J|A|C|S

ARTICLES

Architectural Control of Seeded-Grown Magnetic–Semicondutor Iron Oxide–TiO₂ Nanorod Heterostructures: The Role of Seeds in Topology Selection

Raffaella Buonsanti,[†,‡] Vincenzo Grillo,[§] Elvio Carlino,[||] Cinzia Giannini,[⊥]
Fabia Gozzo,[#] Mar Garcia-Hernandez,[∇] Miguel Angel Garcia,[○] Roberto Cingolani,[◆]
and P. Davide Cozzoli*[,†,‡]

Scuola Superiore ISUFI, Università del Salento, Distretto Tecnologico ISUFI, via per Arnesano km 5, 73100 Lecce, Italy, National Nanotechnology Laboratory (NNL) of CNR-INFM, Unità di Ricerca IIT, via per Arnesano km 5, 73100 Lecce, Italy, INFM-CNR Center s3, Via Campi 213/A, 41100 Modena, Italy, TASC-INFM-CNR National Laboratory, Area Science Park - Basovizza, Building, MM, SS 14, Km 163.5, 34012 Trieste, Italy, Istituto di Crystallografia (IC-CNR), via Amendola 122/O, 70126 bari, Italy, Swiss Light Source, Paul Scherrer Institute, 5232 Villigen PSI, Switzerland, Instituto de Ciencia de Materiales de Madrid, CSIC, C/ Sor Juana Ines de la Cruz 3, Campus de Cantoblanco, 28049 Madrid, Spain, Instituto de Ceramica y Vidrio, CSIC, C/ Kelsen 5, Campus de Cantoblanco, 28049 Madrid, Spain, and Fondazione Istituto Italiano di Tecnologia (IIT), via Morego 30, 16163 Genova, Italy

Received December 7, 2009; E-mail: davide.cozzoli@unile.it

Abstract: A colloidal nonaqueous approach to semiconductor–magnetic hybrid nanocrystals (HNCs) with selectable heterodimer topologies and tunable geometric parameters is demonstrated. Brookite TiO₂ nanorods, distinguished by a curved shape-tapered profile with richly faceted terminations, are exploited as substrate seeds onto which a single spherical domain of inverse spinel iron oxide can be epitaxially grown at either one apex or any location along their longitudinal sidewalls in a hot surfactant environment. The topologically controlled arrangement of the component material lattices, the crystallographic relationships holding between them, and strain distribution across individual heterostructures have been studied by combining X-ray diffraction and absorption techniques with high-resolution transmission electron microscopy investigations. Supported by such structural knowledge, the synthetic achievements are interpreted within the frame of various mechanistic models offering complementary views of HNC formation. The different HNC architectures are concluded to be almost equivalent in terms of surface–interface energy balance associated with their formation. HNC topology selection is rationalized on the basis of a diffusion-limited mechanism allowing iron oxide heterogeneous nucleation and growth on the TiO₂ nanorods to switch from a thermodynamically controlled to a kinetically overdriven deposition regime, in which the anisotropic reactivity offered by the uniquely structured seeds is accentuated under high spatially inhomogeneous monomer fluxes. Finally, the multifunctional capabilities of the heterostructures are highlighted through illustration of their magnetic and photocatalytic properties, which have been found to diverge from those otherwise exhibited by their individual material components and physical mixture counterparts.

1. Introduction

Colloidal inorganic nanocrystals (NCs) with engineered structural and geometric parameters are at the forefront of the current scientific revolution of nanoscience. They serve as model systems for the study of physical-chemical phenomena in nanoscale solids and as indispensable ingredients for the bottom-up development of artificial functional materials, miniaturized devices, and innovative concepts in optoelectronics, biomedicine, and catalysis.[1]

Currently, new challenges are being imposed on nanochemistry research to satisfy the rising demand for advanced generations of wet-chemically synthesized NC-based entities that should not only exhibit reinforced properties, but also demonstrate diversified capabilities to be simultaneously exploitable in multiple applications. One frontier approach envisages

† Università del Salento.
‡ Unità di Ricerca IIT.
§ INFM-CNR Center s3.
|| TASC-INFM-CNR National Laboratory.
⊥ Istituto di Crystallografia.
Paul Scherrer Institute.
∇ Instituto de Ciencia de Materiales de Madrid.
○ Instituto de Ceramica y Vidrio.
◆ Fondazione Istituto Italiano di Tecnologia.

(1) (a) Cozzoli, P. D.; Pellegrino, T.; Manna, L. *Chem. Soc. Rev.* **2006**, *35*, 1195–1208. (b) Buonsanti, R.; Casavola, M.; Caputo, G.; Cozzoli, P. D. *Recent Pat. Nanotechnol.* **2007**, *1*, 224–232. (c) Casavola, M.; Buonsanti, R.; Caputo, G.; Cozzoli, P. D. *Eur. J. Inorg. Chem.* **2008**, 837–854. (d) Caputo, G.; Buonsanti, R.; Casavola, M.; Cozzoli, P. D. Synthetic strategies to multi-material hybrid nanocrystals. In *Advanced Wet-Chemical Synthetic Approaches to Inorganic Nanostructures*; Cozzoli, P. D., Ed.; Transworld Research Network: Kerala, India; pp 407–453.

construction of multicomponent nanoheterostructures, referred to as hybrid NCs (HNCs), in which two or more distinct domains of selected metals, semiconductors, and/or oxides are interconnected through epitaxial bonding interfaces in elaborate spatial configurations. Examples of HNCs with a topologically defined composition span from concentric or eccentric core/shell geometries involving large junctions between the component materials, to oligomer-like architectures made of shape-tailored sections sharing small contact areas.[1,2]

Elaboration of HNCs transcribes a new paradigm in synthetic nanochemistry, whereby higher level of structural-architectural complexity is pursued as a means of boosting the technological potential of conventional nanoparticles beyond the limitations dictated by their compositional and geometric parameters.[1,2] Indeed, HNCs offer enhanced functionality stemming from integration of nonhomologous properties over a unique inorganic platform on which multiple surfaces are chemically addressable at once.[1,2] Electronic interfacing across neighboring domains through the relevant heterojunctions can underlie interesting exchange-coupling mechanisms, often leading to synergistically amplified chemical-physical responses or even emergence of entirely new phenomena.[1–38] Suitable heterostructure engineering is ultimately expected to open up unprecedented scenarios in many applications fields, such as optoelectronics, biomedicine, sensing, catalysis, and fabrication of smart artificial mesoscopic materials, where multimodal imaging, detection, targeting, and therapeutic actions, on one side, and programmable organization of NC-based superlattices, on the other side, are greatly needed.[1–18]

(2) (a) Jun, Y.-w.; Choi, J.-s.; Cheon, J. *Chem. Commun.* **2007**, 1203–1214. (b) Gao, J.; Gu, H.; Xu, B. *Acc. Chem. Res.* **2009**, *42*, 1097–1107.

(3) (a) Kwon, K. W.; Shim, M. *J. Am. Chem. Soc.* **2005**, *127*, 10269–10275. (b) Kwon, K.-W.; Lee, B. H.; Shim, M. *Chem. Mater.* **2006**, *18*, 6357–6363. (c) McDaniel, H.; Shim, M. *ACS Nano* **2009**, *3*, 434–440.

(4) Mokari, T.; Aharoni, A.; Popov, I.; Banin, U. *Angew. Chem., Int. Ed.* **2006**, *45*, 8001–8005.

(5) (a) Shi, W.; Zeng, H.; Sahoo, Y.; Ohulchanskyy, T. Y.; Ding, Y.; Wang, Z. L.; Swihart, M.; Prasad, P. N. *Nano Lett.* **2006**, *6*, 875–881. (b) Franchini, I. R.; Bertoni, G.; Falqui, A.; Giannini, C.; Wang, L. W.; Manna, L. *J. Mater. Chem.* **2010**, published online on Oct 20, 2009, DOI: 10.1039/b915687a. (c) Yang, J.; Elim, H. I.; Zhang, Q.; Lee, J. Y.; Ji, W. *J. Am. Chem. Soc.* **2006**, *128*, 11921–11926. (d) Yang, J.; Peng, J.; Zhang, Q.; Peng, F.; Wang, H.; Yu, H. *Angew. Chem., Int. Ed.* **2009**, *48*, 3991–3995.

(6) (a) Yu, H.; Chen, M.; Rice, P. M.; Wang, S. X.; White, R. L.; Sun, S. *Nano Lett.* **2005**, *5*, 379–382. (b) Wei, Y.; Klajn, R.; Pinchuk, A. O.; Grzybowski, B. A. *Small* **2008**, *4*, 1635–1639.

(7) Shi, W.; Sahoo, Y.; Zeng, H.; Ding, Y.; Swihart, M. T.; Prasad, P. N. *Adv. Mater.* **2006**, *18*, 1889–1894.

(8) (a) Gao, J.; Zhang, B.; Gao, Y.; Pan, Y.; Zhang, X.; Xu, B. *J. Am. Chem. Soc.* **2007**, *129*, 11928–11935. (b) Gu, H. W.; Zheng, R. K.; Zhang, X. X.; Xu, B. *J. Am. Chem. Soc.* **2004**, *126*, 5664–5665.

(9) (a) Saruyama, M.; Kanehara, M.; Teranishi, T. *Chem. Commun.* **2009**, 2724–2726. (b) Teranishi, T.; Saruyama, M.; Kanehara, M. *Nanoscale* **2009**, *1*, 225–228.

(10) (a) Milliron, D. J.; Hughes, S. M.; Cui, Y.; Manna, L.; Li, J.; Wang, L.-W.; Alivisatos, A. P. *Nature* **2004**, *430*, 190. (b) Talapin, D. V.; Nelson, J. H.; Shevchenko, E. V.; Aloni, S.; Sadtler, B.; Alivisatos, A. P. *Nano Lett.* **2007**, *7*, 2951–2959. (c) Zhong, H.; Scholes, G. D. *J. Am. Chem. Soc.* **2009**, *131*, 9170–9171. (d) Carbone, L.; et al. *Nano Lett.* **2007**, *7*, 2942–2950.

(11) (a) Carbone, L.; Jakab, A.; Khalavka, Y.; Sonnichsen, C. *Nano Lett.* **2009**, *7*, 3710–3714. (b) Mokari, T.; Sztrum, C. G.; Salant, A.; Rabani, E.; Banin, U. *Nat. Mater.* **2005**, *4*, 855. (c) Saunders, A. E.; Popov, I.; Banin, U. *J. Phys. Chem. B* **2006**, *110*, 25421–25429. (d) Menagen, G.; Macdonald, J. E.; Shemesh, Y.; Popov, I.; Banin, U. *J. Am. Chem. Soc.* **2009**, *131*, 17406–17411.

(12) Kudera, S.; Carbone, L.; Casula, M. F.; Cingolani, R.; Falqui, A.; Snoeck, E.; Parak, W. J.; Manna, L. *Nano Lett.* **2005**, *5*, 445–449.

(13) Maynadiè, J.; Salant, A.; Falqui, A.; Respaud, M.; Shaviv, E.; Banin, U.; Soulantica, K.; Chaudret, B. *Angew. Chem., Int. Ed.* **2009**, *48*, 1814–1817.

(14) Deka, S.; Falqui, A.; Bertoni, G.; Sangregorio, C.; Poneti, G.; Morello, G.; De Giorgi, M.; Giannini, C.; Cingolani, R.; Manna, L.; Cozzoli, P. D. *J. Am. Chem. Soc.* **2009**, *131*, 12817–12828.

(15) Casavola, M.; Grillo, V.; Carlino, E.; Giannini, C.; Gozzo, F.; Fernandez Pinel, E.; Garcia, M. A.; Manna, L.; Cingolani, R.; Cozzoli, P. D. *Nano Lett.* **2007**, *7*, 1386–1395.

(16) Cheng, C.; Yu, K. F.; Cai, Y.; Fung, K. K.; Wang, N. *J. Phys. Chem. C* **2007**, *111*, 16712–16716.

(17) (a) Wetz, F.; Soulantica, K.; Falqui, A.; Respaud, M.; Snoeck, E.; Chaudret, B. *Angew. Chem., Int. Ed.* **2007**, *46*, 7079–7081. (b) Lin, Z.-H.; Lin, Y.-W.; Lee, K.-H.; Chang, H.-T. *J. Mater. Chem.* **2008**, *18*, 2569–2572. (c) Vinod, T. P.; Yang, M.; Kim, J.; Kotov, N. A. *Langmuir* **2009**, *25*, 3545–13550.

(18) Robinson, R. D.; Sadtler, B.; Demchenko, D. O.; Erdonmez, C. K.; Wang, L.-W.; Alivisatos, A. P. *Science* **2007**, *317*, 355–358.

(19) (a) Buonsanti, R.; Grillo, V.; Carlino, E.; Giannini, C.; Curri, M. L.; Innocenti, C.; Sangregorio, C.; Achterhold, K.; Parak, F. G.; Agostiano, A.; Cozzoli, P. D. *J. Am. Chem. Soc.* **2006**, *128*, 16953–16970. (b) Buonsanti, R.; Snoeck, E.; Giannini, C.; Gozzo, F.; Garcia-Hernandez, M.; Garcia, M. A.; Cingolani, R.; Cozzoli, P. D. *Phys. Chem. Chem. Phys.* **2009**, *11*, 3680–3691.

(20) (a) Cornell, R. M.; Schwertmann, U. *The Iron Oxides: Structures, Properties, Occurrences and Uses*, 2nd ed.; Wiley-VCH: Weinheim, 2003. (b) Laurent, S.; Forge, D.; Port, M.; Roch, A.; Robic, C.; Vander Elst, L.; Muller, R. N. *Chem. Rev.* **2008**, *108*, 2064–2110.

(21) (a) Chun, C. L.; Hozalski, C.; Arnold, W. A. *Environ. Sci. Technol.* **2005**, *39*, 8525–8532. (b) Danielsen, K.; Gland, J.; Hayes, A. *Environ. Sci. Technol.* **2005**, *39*, 756–763. (c) Wiatrowski, H. A.; Das, S.; Kukkadapu, R.; Ilton, E. S.; Barkay, T.; Yee, N. *Environ. Sci. Technol.* **2009**, *43*, 5307–5313. (d) Gorski, C. A.; Scherer, M. M. *Environ. Sci. Technol.* **2009**, *43*, 3675–3680. (e) Williams, A. G. B.; Scherer, M. M. *Environ. Sci. Technol.* **2004**, *38*, 4782–4790. (f) Yavuz, C. T.; Mayo, J. T.; Yu, W. W.; Prakash, A.; Falkner, J. C.; Yean, S.; Cong, L.; Shipley, H. J.; Kan, A.; Tomson, M.; Natelson, D.; Colvin, V. L. *Science* **2006**, *314*, 964–967. (g) Zeng, H.; Fisher, B.; Giammar, D. E. *Environ. Sci. Technol.* **2008**, *42*, 147–152.

(22) (a) Chen, C. T.; Chen, Y. C. *Anal. Chem.* **2005**, *77*, 5912–5919. (b) Li, Y.; Wu, J.; Qi, D.; Xu, X.; Deng, C.; Yang, P.; Zhang, X. *Chem. Commun.* **2008**, 564–566.

(23) (a) Hoffmann, M. R.; Martin, S. T.; Choi, W.; Bahnemann, D. W. *Chem. Rev.* **1995**, *95*, 69–96. (b) Chen, X.; Mao, S. S. *Chem. Rev.* **2007**, *107*, 2891–2959. (c) Fujishima, A.; Zhang, X.; Tryk, D. A. *Surf. Sci. Rep.* **2008**, *63*, 515–582.

(24) (a) Tronc, E.; Jolivet, J.-P.; Lefebvre, J.; Massart, R. *J. Chem. Soc., Faraday Trans.* **1984**, *80*, 2619–2629. (b) Jung, Y.; Choi, J.; Lee, W. *Chemosphere* **2007**, *68*, 1968–1975. (c) Vikesland, P. J.; Heathcock, A. M.; Rebodos, R. L.; Makus, K. E. *Environ. Sci. Technol.* **2007**, *41*, 5277–5283. (d) Jolivet, J. P.; Tronc, E.; Barbe, C.; Livage, J. *J. Colloid Interface Sci.* **1990**, *138*, 465–472.

(25) (a) Beydoun, D.; Amal, R.; Low, G. K. C.; McEvoy, S. *J. Phys. Chem. B* **2000**, *104*, 4387–4396. (b) Beydoun, D.; Amal, R.; Low, G.; McEvoy, S. *J. Mol. Catal. A* **2002**, *180*, 193–200. (c) Gao, Y.; Chen, B. H.; Li, H. L.; Ma, Y. X. *Mater. Chem. Phys.* **2003**, *80*, 348–355. (d) Ao, Y.; Xu, J.; Fu, D.; Shen, X.; Yuan, C. *Sep. Pur. Technol.* **2008**, *61*, 436. (e) Wang, C.; Yin, L.; Zhang, L.; Kang, L.; Wang, X.; Gao, R. *J. Phys. Chem. C* **2009**, *113*, 4008–4011. (f) Belessi, V.; Lambropoulou, D.; Konstantinou, I.; Zboril, R.; Tucek, J.; Jancik, D.; Albanis, T.; Petridis, D. *Appl. Catal., B* **2009**, *87*, 181–189.

(26) (a) Dames, P.; Gleich, B.; Flemmer, A.; Hajek, K.; Seidl, N.; Wiekhorst, F.; Eberbeck, D.; Bittmann, I.; Bergemann, C.; Weyh, T.; Trahms, L.; Rosenecker, J.; Rudolph, C. *Nat. Nanotechnol.* **2007**, *2*, 495. (b) Seo, J.-w.; Chung, H.; Kim, M.-y.; Lee, J.; Choi, I.-H.; Cheon, J. *Small* **2007**, *3*, 850–853. (c) Paunesku, T.; Rajh, T.; Wiederrecht, G.; Maser, J.; Vogt, S.; Stojicevic, N.; Protic, M.; Lai, B.; Oryhon, J.; Thurnauer, M.; Woloschak, G. *Nat. Mater.* **2003**, *2*, 343–346. (d) Tsai, M.-C.; Tsai, T.-L.; Shieh, D.-B.; Chiu, H.-T.; Lee, C.-Y. *Anal. Chem.* **2009**, *81*, 7590–7596. (e) Endres, P. J.; Paunesku, T.; Vogt, S.; Meade, T. J.; Woloschak, G. E. *J. Am. Chem. Soc.* **2007**, *129*, 15760–15761. (f) Paunesku, T.; Vogt, S.; Lai, B.; Maser, J.; Stojicevic, N.; Thurn, K. T.; Osipo, C.; Liu, H.; Legnini, D.; Wang, Z.; Lee, C.; Woloschak, G. E. *Nano Lett.* **2007**, *7*, 596–601.

(27) Buonsanti, R.; Grillo, V.; Carlino, E.; Giannini, C.; Kipp, T.; Cingolani, R.; Cozzoli, P. D. *J. Am. Chem. Soc.* **2008**, *130*, 11223–11233.

(28) Crystallographic tools for Rietveld profile matching and integrated intensity refinements of X-ray and/or neutron data; available online at http://wwwold.ill.fr/dif/Soft/fp/php/downloads.html.

(29) Hÿtch, M. J. *Microsc. Microanal. Microstruct.* **1997**, *8*, 41–57.

(30) Grillo, V. STEM-CELL; available online at http://tem.s3.infm.it/ software.

The synthesis of HNCs in colloidal media poses several major obstacles to surmount. Controllable HNC fabrication indeed requires that the relevant material component domains should evolve under thermodynamic and kinetic regimes guaranteeing a surface-interface energy balance favorable to creation of bonding connections between dissimilar crystal lattices.[1,2] One widely exploited approach to achieve this goal relies on the so-called "seeded growth", whereby preformed NCs serve as primary nucleation centers that can accommodate deposition of secondary inorganic portions of different materials from the respective molecular precursors.[1,2] The large variety of elaborate HNCs, which has so far become available, supports the general applicability and effectiveness of this synthetic tool. Nevertheless, despite the apparent technical simplicity of seeded techniques, development of versatile protocols that can allow deliberate selection of distinct spatial arrangements for heterostructures made of a given material association yet remains one of the most unsatisfactorily addressed issues. Access to HNCs in nonequivalent configurations within the frame of the same synthetic scheme has in fact been proven to be viable in a few cases only, whereby topology switchability has often been achieved to the detriment of a limited size range of geometric parameters over which the component material domains can be tailored. Examples include binary and ternary hetero-oligomers of Fe₃O₄—CdS,[3] Au—InAs,[4] Au—PbS(or Te),[5] Au—Fe₃O₄,[5a,6] PbS(or Se)—Au—Fe₃O₄,[5a,7] FePt—CdS(or Se),[8] and PdS$_x$—CdS[9] in either core@shell, peanut-, or dumbbell-like configurations, linear and/or branched architectures based on CdX materials (X = S, Se, Te),[10] heterostructures made of site-selectively decorated rod-like sections, such as of CdS(or Se)—Au,[11] CdS(or Se)—PbSe,[12] CdSe—Co,[13] CdSe@CdS—Au(or Co),[11a,14] TiO₂—Co,[15] TiO₂—ZnO,[16] Au—Co (or Te),[17] and striped CdS—Ag₂S nanorods.[18]

Identification of pathways to HNC topology selection is intrinsically challenging, because the ultimate heterostructure geometry and configuration can transcribe the interplay of heterogeneous nucleation with other complex mechanisms, such as solid-state atomic diffusion or exchange,[4,5,18] redox proces-

ses,[5,11] photoinduced or thermal activation,[11] electrochemical ripening,[11b,c] phase segregation,[9] and crystal-oriented attachment.[5a,9] Current expertise remains hindered by an insufficient understanding of the genuine impact of the inherent characteristics of the seeds, such as their crystal structure,[6b,10b–d,14] size/shape,[3,5,10c] faceting,[5,7,11–15] and surface defects,[11] on the evolution of HNCs thereof when significant interfacial polarization[6a,17c] and misfit strain[3,5a,6,7,9a,15,18] intervene at the relevant heterojunctions. Unravelling how these factors determine the preference of foreign material domains to be implanted onto distinct locations of seeds under operation of kinetically driven deposition processes[3c,10a,d] is an essential prerequisite to achieving increased level of synthetic sophistication and predictable functionalities.[1,2] As of today, the most ambitious objective in HNC development remains to innovate current preparative routes, which most commonly rely on empirically determined sets of optimal reaction conditions, by rational synthetic criteria founded on deep structural insight and solid mechanistic knowledge.[1]

In this work, we demonstrate a leap forward in the topological control of HNCs belonging to the yet scarcely tackled realm of heterostructures entirely made of transition-metal oxides, on which synthetic progress has, in fact, been limited, as compared to other material associations.[1c,16,19] We address the wet-chemical fabrication and characterization of novel HNC architectures-based semiconductor TiO₂ and ferromagnetic spinel iron oxide (henceforth referred to as Fe$_x$O$_y$), two technologically important materials that hold great technological potential as adsorptive,[20–23] catalytic,[20,23,24] and (photo)catalytic platforms,[23,25] and as tools for biomedical diagnostics and therapeutics.[20b,26] Beyond conventional magnetically addressable core/shell TiO₂/Fe$_x$O$_y$ composite architectures, our group has recently reported the synthesis of HNCs individually comprising a single rod-shaped TiO₂ section longitudinally decorated with one or more Fe$_x$O$_y$ spherical portions, respectively.[19] As a major drawback, the relative domain positioning could not be controlled and/or interfacial strain dictated the size range over which the heterostructure geometric parameters could be adjusted.[19]

Using the TiO₂/Fe$_x$O$_y$ couple as a model material platform for heteroepitaxial growth via colloidal nonaqueous seeding techniques, herein we show that the combination of accurate seed engineering with appropriate reaction pathways, capable of accentuating anisotropic reactivity, allows a higher degree of flexibility in the selection of nonquivalent HNC architectures. These concepts are illustrated through the synthetic outcome of a robust two-step strategy by which TiO₂—Fe$_x$O$_y$ heterodimer HNCs can be synthesized with controlled topologies and geometric parameters independently tunable over a wide size range. This colloidal system is particularly suitable to address the inherent impact of the TiO₂ seed structure on the formation of TiO₂—Fe$_x$O$_y$ heterostructures thereof, as no redox or atomic exchange reactions complicate structural-compositional characterization and mechanistic understanding.[1,5,11,18] Our approach exploits brookite TiO₂ nanorods, distinguished by a specific shape-tapered profile and arrow-like terminations, as anisotropically reactive seeds in a hot surfactant mixture to which an organometallic iron precursor is controllably supplied. It is demonstrated that selective heterogeneous nucleation and growth of a single cubic-phase iron oxide domain can be attained at either one apex or at any location along the longitudinal sidewalls of the nanorod substrates. The synthetic achievements have been authenticated by combining X-ray diffraction and absorption measurements with high-resolution transmission

(31) Hÿtch, M. J.; Snoeck, E.; Kilaas, R. *Ultramicroscopy* **1998**, *74*, 131–146.

(32) (a) Cozzoli, P. D.; Curri, M. L.; Agostiano, A. *Chem. Commun.* **2005**, 3186–3188. (b) Jakob, M.; Levanon, H.; Kamat, P. V. *Nano Lett.* **2003**, *3*, 353–358. (c) Subramanian, V.; Wolf, E. E.; Kamat, P. V. *J. Am. Chem. Soc.* **2004**, *126*, 4943–4950.

(33) (a) Casula, M. F.; Jun, Y. W.; Zaziski, D. J.; Chan, E. M.; Corrias, A.; Alivisatos, A. P. *J. Am. Chem. Soc.* **2006**, *128*, 1675–1682. (b) Park, J.; An, K.; Hwang, Y.; Park, J.-G.; Noh, H.-J.; Kim, J.-Y.; Park, J.-H.; Hwang, N.-M.; Hyeon, T. *Nat. Mater.* **2004**, *3*, 891. (c) Park, J.; Lee, E.; Hwang, N.-M.; Kang, M.; Chul Kim, S.; Hwang, Y.; Park, J.-G.; Noh, H.-J.; Kim, J.-Y.; Park, J.-H.; Hyeon, T. *Angew. Chem., Int. Ed.* **2005**, *44*, 2872–2877. (d) Kwon, S. G. P., Y.; Park, J.; Angappane, G., Y.; Jo, Y.; Hwang, N.-M.; Park, J.-H.; Hyeon, T. *J. Am. Chem. Soc.* **2007**, *129*, 12571–12584.

(34) (a) Jun, Y.-w.; Choi, J.-s.; Cheon, J. *Angew. Chem., Int. Ed.* **2006**, *45*, 3414–3439. (b) Manna, L.; Kudera, S. Mechanisms underlying the growth of inorganic nanoparticles in the liquid phase. In *Advanced Wet-Chemical Synthetic Approaches to Inorganic Nanostructures*; Cozzoli, P. D., Ed.; Transworld Research Network: Kerala, India; pp 1–53.

(35) (a) Hytch, M. J.; Plamann, T. *Ultramicroscopy* **2001**, *87*, 199–212. (b) Seitz, H.; Ahlborn, K.; Seibt, M.; Schroeter, W. *J. Microsc.* **1997**, *190*, 184.

(36) (a) Peng, X. *Adv. Mater.* **2003**, *15*, 459–463. (b) Peng, Z. A.; Peng, X. G. *J. Am. Chem. Soc.* **2001**, *123*, 1389–1395.

(37) (a) Mullins, W. W.; Sekerka, R. F. *J. Appl. Phys.* **1964**, *35*, 444–451. (b) Mullin, J. W. *Crystallization*, 4th ed.; Butterworth-Heinemann: Oxford, 2001.

(38) Manna, L.; Scher, E. C.; Alivisatos, A. P. *J. Am. Chem. Soc.* **2000**, *122*, 12700–12706.

electron microscopy investigations, complemented by analysis of lattice fringe contrast amplitude and displacement. These studies have enabled detailed assessment of the topologically defined arrangement of the HNCs, determination of the crystallographic relationships holding between the component material domains, and mapping of lattice strain distribution across individual heterostructures. With the support of such structural knowledge, the experimental results are interpreted within the frame of various models offering complementary mechanistic views of HNC formation. The different HNC architectures are concluded to be approximately equivalent in terms of the surface-interface energy change associated with their formation. We rationalize the possibility of selecting HNC topology on the basis of a diffusion-controlled mechanistic picture allowing Fe_xO_y heterogeneous nucleation on the NR seeds to switch from a thermodynamically controlled to a kinetically overdriven deposition regime. It is proposed that the chemical accessibility of the seeds is governed by the spatial inhomogeneity of the chemical potential environment around them, whereby the anisotropic reactivity offered by the unique structural features of the NR apexes is conveniently accentuated under high fluxes of monomer species. Finally, the multifunctional potential of the $Fe_xO_y-TiO_2$ heterostructures is highlighted through investigation of their rich magnetic and photocatalytic properties, which are found to diverge from those otherwise exhibited, respectively, by their individual material components or physical mixtures thereof.

2. Experimental Section

2.1. Materials. All chemicals were of the highest purity available and were used as received. Titanium(IV) chloride ($TiCl_4$, 99.999%), iron pentacarbonyl ($Fe(CO)_5$, 98%), dodecan-1,2-diol ($C_{12}H_{24}(OH)_2$ or DDIOL, 90%), oleic acid ($C_{17}H_{33}CO_2H$ or OLAC, 90%), oleyl amine ($C_{17}H_{33}NH_2$ or OLAM, 70%), 1-octadecene ($C_{18}H_{36}$ or ODE, 90%), fullerene (C_{60}, 99.5%), and Uniblue A (UBA, sodium salt; the molecular structure is reported in Figure S1 of the Supporting Information) were purchased from Aldrich. All solvents used were of analytical grade.

2.2. Synthesis Procedures. All syntheses were carried out under nitrogen atmosphere using a standard Schlenk line setup.

Preparation of TiO_2 Nanorod Seeds. Size-tunable brookite TiO_2 nanorods (*b*-TiO_2 NRs) with tapered shape were synthesized by using a recently developed protocol with minor modifications.[27] Briefly, 3 g of ODE, 10 mmol of OLAM, and 1 mmol of OLAC were loaded into a three-neck flask and degassed at 120 °C for 30 min, after which the mixture was cooled to 50 °C under N_2 flow. At this point, 1 mmol of $TiCl_4$ was added, and the flask was heated up to 280 °C at a ramp rate of ~20 °C/min and kept at this temperature for 30 min. Next, the reaction could be either halted by removing the heating mantle and allowing rapid cooling, or continued upon alternating additions of a 0.5 M OLAC/ODE solution (injected in single portion) and of a 0.5 M $TiCl_4$/ODE solution (delivered at a constant rate of 0.1 mL/min by means of a syringe pump). The NR size could be enlarged by injecting increasing amounts of the secondary $TiCl_4$/OLAC reactants up to a maximum of ~20 mmol of $TiCl_4$. After the synthesis, the *b*-TiO_2 NRs were precipitated under ambient atmosphere upon addition of a 1:1 v/v 2-propanol:acetone mixture, separated by centrifugation, and then washed three times with acetone to remove any reactant and solvent residuals. The purified NRs were used to prepare stable *b*-TiO_2 seed stock solutions (in $CHCl_3$ or toluene), the concentration of which was checked by ICP-AES analysis prior to further use.

Synthesis of *b*-$TiO_2-Fe_xO_y$ HNCs. HNCs made of joint *b*-TiO_2 and Fe_xO_y sections were synthesized by adapting literature protocols developed for other types of TiO_2 seeds.[19] Calibrated amounts of the *b*-TiO_2 NR stock solution, DDIOL, OLAM, and OLAC were

codissolved in 10 mL of ODE in a 50 mL three-neck flask. The mixture was pumped to vacuum for 30 min at 120 °C, after which it was heated under N_2 flux to 280 °C. After 15 min equilibration, 1 mL of a room-temperature 0.1−1 M $Fe(CO)_5$ solution in previously degassed ODE was rapidly injected into the vigorously stirred seed-containing mixture where the TiO_2 concentration could vary in the 0.001−0.01 M range. In standard matchstick-generating syntheses, the initial TiO_2:OLAC:OLAM:DDIOL molar ratio was optimized to 1:1.5:0.75:1.25,[19] while the $Fe(CO)_5$:TiO_2 molar ratio generally ranged from 1:1 to 10:1. The $Fe(CO)_5$ injection caused a sudden temperature drop of ~20−40 °C, after which the temperature was allowed to slowly recover to 280 °C and maintained at this level. The onset of iron oxide nucleation, marked by a rapid darkening of the solution, was characterized by an induction time of 1−3 min, which was inversely proportional to the amount of $Fe(CO)_5$ injected. After heating for 1 h, the reaction could be either halted or continued upon delivering an additional 2−10 mL of $Fe(CO)_5$:OLAC feedstock precursor (prepared in a separated flask under N_2 at a Fe:OLAC molar ratio of 1:1.5) at a rate of 0.1 mL/min by means of a syringe pump. Finally, the flask was allowed to cool to 130 °C and exposed to air for an additional 1 h to complete Fe_xO_y oxidation. The HNC product was separated from the growing mixture upon 2-propanol addition and subsequently subjected to three cycles of redissolution in $CHCl_3$ and precipitation with acetone to wash out reactant residuals. The final hydrophobically capped HNCs were fully dispersible in a variety of nonpolar solvents (such as hexane, toluene, or chloroform), providing optically clear colloidal solutions.

Synthesis of *b*-TiO_2/Fe_xO_y Physical Mixtures. For comparison purposes, corresponding *b*-TiO_2/Fe_xO_y physical mixtures were prepared by mixing at room temperature appropriate volumes of solutions containing purified NRs and Fe_xO_y NCs synthesized in an independent step (in the absence of seeds using a 3-fold higher reactant concentration).

2.3. Characterization. 2.3.1. Elemental Analysis. The Ti and Fe atomic contents of the samples were measured by inductively coupled plasma atomic emission spectroscopy (ICP-AES) measurements with a Varian Vista AX spectrometer. The samples for analyses were digested in concentrated HCl/HNO_3 (3/1 v/v). Unless otherwise stated, the concentration of TiO_2 and Fe_xO_y was expressed in terms of TiO_2 and Fe_2O_3 molecular units. When needed, the molecular TiO_2 concentration was translated into TiO_2 seed concentration (expressed as number of seeds per unit volume) by considering the average mass of a single NR calculated on the basis of the mean NR length and diameter and the density of bulk brookite (4.12 g/cm³).

2.3.2. Steady-State UV−Vis Absorption Spectroscopy. UV−vis absorption spectra were recorded using a Cary 5 Varian UV/vis near-IR spectrophotometer.

2.3.3. X-ray Diffraction (XRD). Synchrotron radiation XRD (SR-XRD) experiments were performed at the Swiss Light Source Materials Science Beamline. The samples for analysis were dry nanocrystal powders loaded into 0.4 mm capillaries and spun at approximately 10 Hz to improve the count statistics. Full diffraction patterns were collected in Debye−Scherrer transmission geometry using the Si(111) multicrystal analyzer detector. The photon wavelength was set at 0.620974 ± 0.000015 Å (or equivalently E = 19.965405 ± 0.000467 keV), as determined using a NIST Si 640c standard. The 2θ zero offset was negligible (0.000652° ± 0.000014°). The instrumental function was practically insignificant relative to the intrinsic contribution of the nanocrystalline samples to reflection broadening.

Data Fitting. A whole profile XRD fitting was performed by using the software FULLPROF based on the Rietveld method, which takes into account NC shape anisotropy by means of spherical harmonics.[28] The initial crystallographic data used for the fits were the following bulk values: a *I*41/*amd* space group and unit cell parameters $a = b = 3.7852$ Å, $c = 9.5139$ Å for anatase TiO_2; a *Pbca* space group and unit cell parameters $a = 9.174$ Å, $b = 5.449$

Å, $c = 5.138$ Å for brookite TiO₂; a $P43_32$ space group and a unit cell size $a = b = c = 8.3457$ Å for γ-Fe₂O₃ (maghemite); and a Fd-3m space group and unit cell size $a = b = c = 8.3965$ Å for Fe₃O₄ (magnetite). The fits were accomplished under the initial assumption that the NRs could be made of anatase and/or brookite TiO₂, while the HNCs could be composed of TiO₂/γ-Fe₂O₃, TiO₂/Fe₃O₄, or TiO₂/Fe₃O₄/γ-Fe₂O₃ mixtures. The accuracy of the fits was evaluated on the basis of a goodness-of-fit statistical indicator (GOF) that takes the value of 1 for an ideal fit. Given the high count rate of the pattern intensity, GOF values of <5−6 were considered to be satisfactory. For the sake of comparison, refined cell parameters were calculated for b-TiO₂ in the starting NRs and in HNCs thereof, which allowed estimating changes in b-TiO₂ unit cell volume following Fe$_x$O$_y$ overgrowth.

2.3.4. X-ray Absorption Spectroscopy. X-ray absorption near-edge structure spectroscopy (XANES) measurements at the Fe *K*-edge energy were performed at room temperature in transmission mode at the BM25 Spanish CRG Beamline (SpLine) of the European Synchrotron Radiation Facility (ESRF). Two gas ionization chambers, filled with nitrogen and argon, were used to measure the incident and the transmitted beam, respectively. Samples for analysis were in powdered form and placed onto a kapton tape located in the beam path at room temperature. The powder amount to be mounted was calculated so as to achieve similar signal intensity for all of the samples. Several scans were taken to improve the signal-to-noise ratio. Bulk γ-Fe₂O₃ and Fe₃O₄ powders were also measured for comparison purposes. Data were normalized applying the same normalization parameters for all of the spectra by means of an in-house software (Athena).

2.3.5. Transmission Electron Microscopy (TEM). Low-resolution TEM images were recorded with a Jeol Jem 1011 microscope operating at an accelerating voltage of 100 kV. Phase-contrast high-resolution TEM (HRTEM) experiments were performed by using a Jeol 2010F TEM/STEM microscope operating at 200 keV, which corresponded to an electron wavelength of 0.00251 nm. The objective lens had a spherical aberration coefficient of 0.47 ± 0.01 nm and hence a resolution at optimum defocus of 0.19 nm. Samples for analysis were prepared by dropping a dilute NR or HNC solution in toluene onto carbon-coated copper grids and then allowing the solvent to evaporate.

Crystal-Phase Mapping. Crystal-phase maps of the nanostructures were constructed by analyzing the local amplitude of the HRTEM periodicities characteristic of each crystal phase. To this aim, the Fourier transform of the HRTEM image was treated according to the approach developed by M. J. Hÿtch, described elsewhere.[19a,29] The results were translated into false-color maps, in which areas featured by the same periodicity were represented by a fixed chromatic scale based on a different color for each crystal phase. The topological variations of the color intensity and hue, being proportional to the local amplitude of the concerned HRTEM fringes, were expressed relative to a percentage chromatic scale, whereby 100% was assigned to the location across the nanostructure at which the intensity of the concerned fringes was maximum, while 0% corresponded to the intensity of the same fringes in a region outside the crystal lattice.

Strain Mapping. To probe strain effects induced in the TiO₂ NRs upon formation of b-TiO₂−Fe$_x$O$_y$ heterojunctions, in-plane b-TiO₂ strain maps were calculated both for the bare NRs and for the HNCs thereof using the program STEM_CELL[30] that is based on the well-established geometric phase analysis (GPA) developed by M. J. Hÿtch et al.[19b,27,31] The GPA technique allows the relative extent of lattice fringe distortion across the nanostructures to be evaluated with respect to an "unstrained" area within the two-dimensional projected lattice, which is taken as a reference. In the case of the bare NRs, the reference area was selected in the middle of the nanostructure, while in the case of b-TiO₂−Fe$_x$O$_y$ HNCs, the reference area was selected in a region of the TiO₂ section, which was located at least ~10 nm away from the interface shared with the Fe$_x$O$_y$ domain. The suitability of the reference choice was

checked by verifying that the strain level converged to a constant value thereon. The results of the analyses were used to construct false-color strain maps, each tracing the topological changes associated with a specific lattice distortion component that contributed to the overall strain: (i) fringe deformation (dilatation/contraction) in the direction perpendicular (D_{xx}) or parallel to the long NR axis (D_{yy}), fringe rotation (R_{xy}), and shear strain (S_{xy}).

2.3.6. Magnetic Characterization. Magnetic measurements were performed on dry HNC or NR/Fe$_x$O$_y$ mixture powder samples, mounted on identical holders, using a MPMS Quantum Design SQUID magnetometer. Samples were handled under air using plastic tools and gloves to avoid metal contamination at any step of sample manipulation. The thermal dependence of the magnetization was measured after zero-field cooling (ZFC) under an applied field of 50 Oe. Magnetization curves were measured at 5 and 300 K applying a magnetic field up to 20 KOe. The results were normalized to the iron oxide mass in the samples (assuming a Fe₂O₃ stoichiometry), estimated by ICP-AES measurements.

2.3.7. Photocatalytic Experiments. The photocatalytic activity of the heterostructures was assessed by probing their photoinduced charging capability, according to established approaches.[32] All experiments were carried out using anhydrous solvents under nitrogen atmosphere in a glovebox. Briefly, 1 cm quartz cuvettes were filled with a solution containing the desired amount of purified nanostructures (either b-TiO₂ NRs, HNCs, corresponding physical mixture, or bare Fe$_x$O$_y$ NCs) dissolved in CHCl₃ (or toluene) and ethanol at 80:20 v/v. The typical concentrations were in the range: [TiO₂] = 0.1−10 mM, [Fe$_x$O$_y$] = 0.1−1 mM, respectively. The cuvettes were sealed by a Teflon-faced rubber cap, transferred out of the glovebox, and illuminated for 1−3 h with a 365 ± 10 nm He:Hg lamp (400 μW/cm²) positioned at a distance of 5 cm. To titrate electrons stored on the nanostructured photocatalysts, 10−100 μL of concentrated solution of acceptor molecules, UBA[32a] in dissolved in ethanol or C₆₀[32b,c] dissolved in CHCl₃, was syringed through the septum of the cuvette under strict exclusion of air. The reaction course was followed spectrophotometrically by recording differential spectra after each addition. Either the unirradiated or the preirradiated photocatalyst solution was used as the reference. In complementary sets of experiments, reductive decolorization of UBA was accomplished under continuous light irradiation in the presence of the selected photocatalysts.

3. Results

We have realized the selective synthesis of topologically controlled binary metal−oxide HNCs by devising a robust seeded-growth strategy that involves the following main steps. First, a high-temperature surfactant-assisted nonhydrolytic route[27] is exploited to prepare uniform, size-tunable b-TiO₂ NRs that are elongated in the c-axis direction of the orthorhombic brookite lattice and specifically possess a pronounced tapered profile with structurally dissimilar arrow-shaped terminations. In a subsequent separate step, b-TiO₂−Fe$_x$O$_y$ HNCs are generated upon reacting thoroughly purified b-TiO₂ seeds dissolved in a ternary ligand environment (composed of OLAM, OLAC, and DDIOL in ODE) with a calibrated volume of a Fe(CO)₅/ODE solution injected at 290 °C under inert atmosphere.[28,33] On demand, supplementary additions of a secondary Fe(CO)₅: OLAC feedstock mixture at judiciously slow rate can be performed to sustain enlargement of the Fe$_x$O$_y$ domains to the desired size. After reaction completion and extraction/purification procedures, the final surfactant-coated hydrophobic nano-heterostructures result in being fully soluble in a variety of nonpolar solvents (such as hexane, toluene, or chloroform), providing optically clear solutions.

3.1. Synthesis and Structural Analysis of TiO₂ Seeds. We have first carried out an in-depth size-morphological and

structural study of the particular b-TiO$_2$ NRs, which have been exploited as starting substrates for Fe$_x$O$_y$ overgrowth. Such knowledge is an underlying prerequisite to rationalization of their inherent site-selective seeding capabilities in the process of Fe$_x$O$_y$ deposition.

The b-TiO$_2$ NRs were prepared via OLAM-induced aminolysis of a titanium oleate complex that was formed upon reacting TiCl$_4$ in ODE-diluted OLAC:OLAM mixtures at 280 °C under inert atmosphere.[27] The low-magnification TEM gallery in Figure 1 summarizes the outcome of various syntheses performed by decomposing increasingly larger amounts of equimolar TiCl$_4$:OLAC reactants at a fixed value of the OLAM content in the reaction flask. Single-step preparations at relatively low precursor loading led to roughly ellipsoidal NRs frequently characterized by an asymmetric short axis shrinking in proximity of their terminal sections, which conferred them delicate profiles as diverse as tear-, bullet-, and nail-like (Figure 1a). Upon feeding with extra reactants, the NRs acquired progressively larger volumes and tended to adopt a more tapered shape with pronounced longitudinal bending, while still exhibiting sharp apexes with variable shapes (Figure 1b–d). Proper regulation of the synthesis parameters allowed the nanostructure diameter and the length to be adjusted in the 3–10 nm and 30–180 nm intervals, respectively, which ultimately afforded NRs with aspect ratio easily tunable from ∼4 to ∼15 (Figure 1a–d). In this nonaqueous system, the low crystal symmetry of brookite lattice and facet-competitive surfactant adhesion on the growing nanostructures underlie anisotropic growth,[34] while the particular morphological evolution of the b-TiO$_2$ NRs toward an accentuated tapered habit is specifically promoted by a low OLAM concentration in the starting environment, which then becomes progressively enriched with OLAC along the course of the secondary TiCl$_4$:OLAC feedstock injections.[27,34]

The crystal phase composition b-TiO$_2$ NRs was confirmed by SR-XRD analysis of powder samples. The representative pattern in Figure 2 (trace a), corresponding to NRs with short/long axis of 5 ± 0.8 nm/60 ± 4 nm, matches well with the profile of the bulk brookite (orthorhombic) crystalline phase, as highlighted by the emergence of the distinctive (121), (022), and (221) reflections, not otherwise found for the structurally similar anatase polymorph.[23b] Deviations in the relative peak intensity ratio, as compared to that found in the bulk pattern, and inhomogeneous line broadening arise from the inherent shape anisotropy of the NRs,[23b,27] as confirmed by satisfactory fitting of the experimental SR-XRD patterns obtained by means of a Rietvel-based software program.[28] Similar results were reported for NRs possessing varying geometric features in the 20–200 nm range.

Phase-contrast HRTEM investigations, supported by fast Fourier transform (FFT) and fringe analyses on the relevant images, disclosed important structural details of the as-synthesized seeds. The collected data, summarized in Figure 3, demonstrate that the NRs were indeed constituted of single-crystalline TiO$_2$ expanded along the c-axis of the orthorhombic brookite structure (Figure 3a,d,g–n). The fact that the local FFTs calculated from different regions across the NR length slightly diverge from each other, while often displaying elongated diffraction spots (bottom insets in Figure 3a,d,o–w), correlates with the noticeable crystal deformation that is associated with the longitudinal curvature of the NRs.[27]

To gain a deeper insight into the degree of lattice strain tolerated by the NRs, we traced local changes in the HRTEM contrast amplitude of the visible fringes and assessed the extent

of their spatial displacement through suitable analysis techniques relying on the treatment of the Fourier transform components of the HRTEM images.[19a,29–31,35]

First, point-to-point variations in the visibility of the most prominent crystal-phase periodicities across the NRs were visualized into topological crystal-phase maps[19a,27,35] (Figure 3b,e). These maps evidenced appreciable alterations in the HRTEM contrast amplitude (up to a 40–50% decrease) of the concerned lattice planes across the NR length, as preliminarily grasped from the parent HRTEM image (additional examples can be found in Figure S2 of the Supporting Information). These findings can be interpreted by considering that local atomic plane tilting associated with in- and/or out-of-plane longitudinal bending of the NRs results in misalignment of portions of the nanostructures relative to their exact zone axis condition and, consequently, in attenuation of the relative HRTEM contrast intensity.

Second, the detailed distribution of strain across the NRs was probed by means of the GPA approach.[30,31,35] The analysis of HRTEM contrast variation by this methodology allows decoupling the overall tension experienced by the crystal lattice into its main projected components. Therefore, the percentage degrees of (i) in-plane fringe deformation in the direction perpendicular or parallel to the long NR axis (D_{xx} and D_{yy}, respectively), (ii) fringe rotation (R_{xy}), and (iii) shear strain (S_{xy}) were evaluated with respect to a reference area (to which D_{xx} = D_{xy} = 0%, R_{xy} = 0°, and S_{xy} = 0% were assigned) arbitrarily selected in the nanostructure center, and used to construct corresponding topological maps of strain distribution. In these maps, the color scale and the signs "+" and "−" denote, respectively, the extent and the direction of the change of the particular strain component concerned, relative to the reference. Taking into account the inherent limits imposed by electron delocalization and statistic noise in the HRTEM image,[35] the ultimate accuracy achievable in strain determination by GPA was assessed to be the order of less than 1% (see Appendix in the Supporting Information). The representative data reported in Figure 3c,f show that the D_{xx}, D_{yy}, and S_{xy} components in the NRs generally exhibit only minor oscillations (i.e., of the same order as the GPA accuracy) that are randomly localized across their length. Differently, the R_{xy} map reveals a monotonic excursion of the degree of lattice rotation, which overall reaches up to about 9–14°, as the concerned fringes span the entire NR section from one tip to the opposite one. Therefore, it could be concluded that the b-TiO$_2$ lattice of the bare seeds was affected by insignificant dilatation or contraction, while the sole source of non-negligible strain stemmed from plane bending along the c-axis, which accounted for the NR longitudinal curvature.

The surface faceting of the NRs was analyzed in depth (Figure 3a,d,g–n). Under the observed projections, the most developed longitudinal sidewalls that enclosed the NRs were generally found to be relatively smooth facets of the (2,1,0), (2,2,0), and (1,0,0) type families. On the other hand, the surface arrangement at the apex regions showed a richer structural diversity that appeared to depend on the NR size. The smaller NRs (Figure 3a,d) generally terminated at one or both sides with highly atomically corrugated or stepped tips, on which defined sets of facets could not be unambiguously identified due to their exceedingly small extension and the intrinsic limitations imposed by fringe delocalization effects. Medium-sized NRs (Figure 3g–i,l,m) generally carried only one extremely rough apex with either completely indeterminate faceting or with high-index
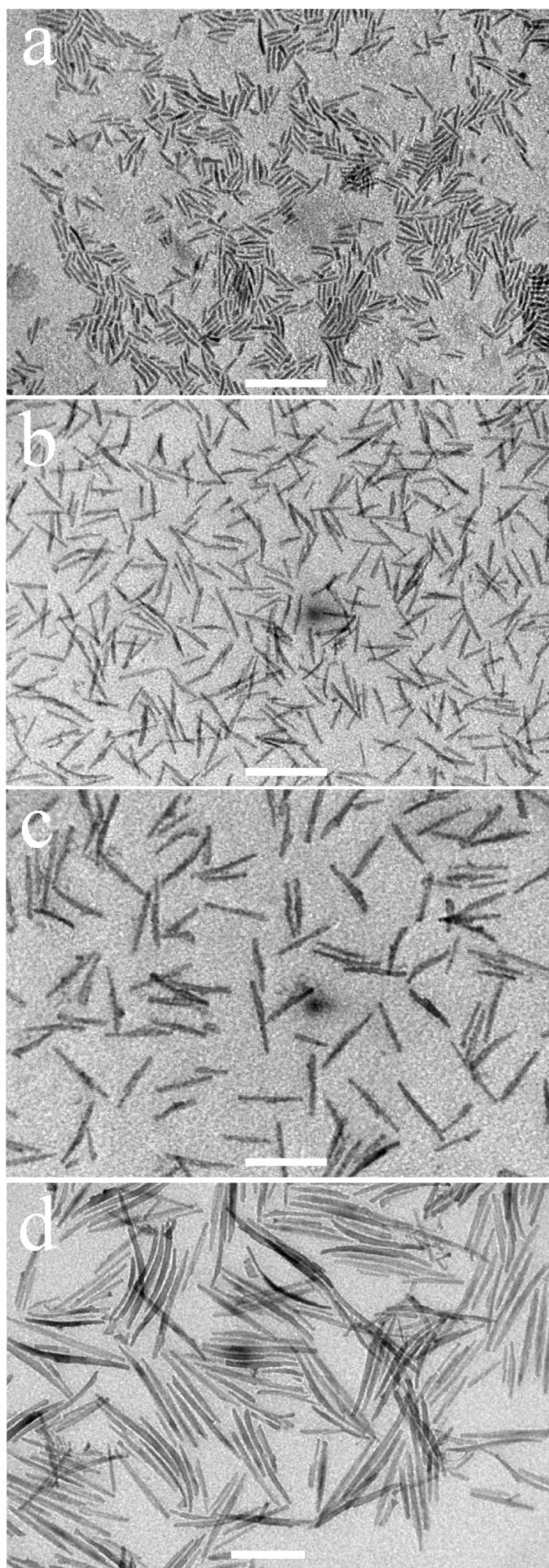
Figure 1. Low-magnification TEM overview of tapered *b*-TiO₂ NRs (seeds) with different geometric parameters synthesized by reacting a total amount of 1 mmol (a), 8 mmol (b), 14 mmol (c), and 18 mmol (d) of TiCl₄, respectively, in OLAM:OLAC:ODE mixtures (white scale bar = 100 nm).
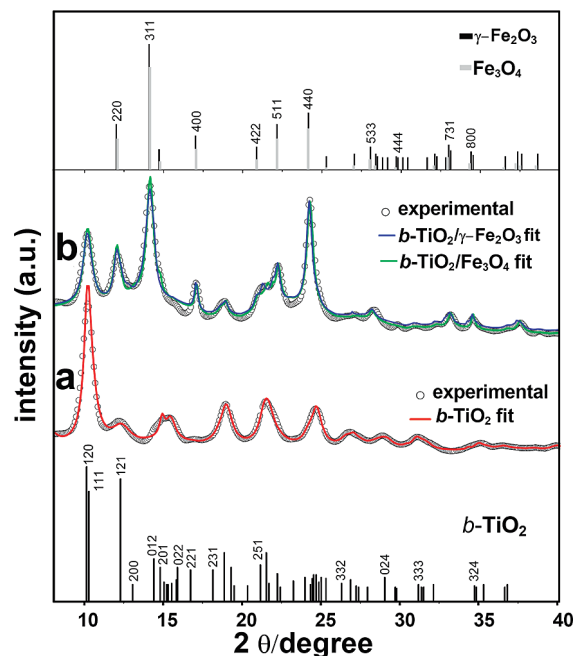
Figure 2. Representative SR-XRD patterns of ~5 ± 0.8 nm × ~60 ± 4 nm *b*-TiO₂ NR seeds (curve a); *b*-TiO₂/Fe$_x$O$_y$ HNCs, grown from such NR seeds, which are functionalized with Fe$_x$O$_y$ domains of ~10 nm (curve b), along with the reference pattern for bulk TiO₂ brookite (*b*-TiO₂), magnetite (Fe₃O₄), and maghemite (γ-Fe₂O₃). The experimental curves (black) are compared to Rietveld-based fits accomplished assuming the existence of *b*-TiO₂ (curve a) or mixtures of *b*-TiO₂/γ-Fe₂O₃ or *b*-TiO₂/Fe₃O₄ (curve b). The refined cell parameters calculated were as follows: $a = 9.168964$ Å, $b = 5.454103$ Å, $c = 5.139221$ Å for *b*-TiO₂ in the HNCs and $a = 9.246865$ Å, $b = 5.417928$ Å, $c = 5.182731$ Å for *b*-TiO₂ in the starting NRs, respectively. The GOF indicators were <2–3 in all cases. Any possible anatase contamination was verified to be of the order of 2–3%, which is within the accuracy of the fitting procedure and, therefore, considered to be negligible.

surfaces, such as of the (1,1,1), (2,1,1), (212), (h,0,2) type (with $h = \pm3, \pm4$), while somewhat (0,0,1) type facets were most commonly deduced at the opposite side. The pronounced asymmetric nanostructure sharpening already appreciable in the low-magnification TEM galleries was consistent with these findings (cf., Figure 1). As their average size and aspect ratio increased, the NRs exhibited a higher degree of surface regularity, which transcribed into the availability of proportionally more extended facets of the aforementioned families at both terminations (Figure 3j,k,n). It was remarkable that, in most cases, the NRs were individually distinguished by substantially different structural arrangements at their apexes (additional examples of NR faceting can be found in Figures S2−S4 in the Supporting Information).

These analyses of faceting above show that the NR surface composition deviates from that predicted theoretically on the basis of the Wulff construction, according to which most of the surface in equilibrium-shape unpassivated brookite crystals should be distributed among (1,1,1), (2,1,0), (0,1,0), and reconstructed (0,0,1) type facets. For example, the observed NR sharpening highlights the tendency of the system to eliminate the unstable basal (0,0,±1) sides, which are expected to develop the fastest, in favor of slower-growing higher-index oblique facets, such as, for example, of the (2,1,1) and (2,1,2) type,[1a,34,36−38] as indeed observed by us. In addition, the asymmetric profile of NR tapering unequivocally points to dissimilar growth rates along the two opposite directions of the *c*-axis, which would contrast with expectations based on the
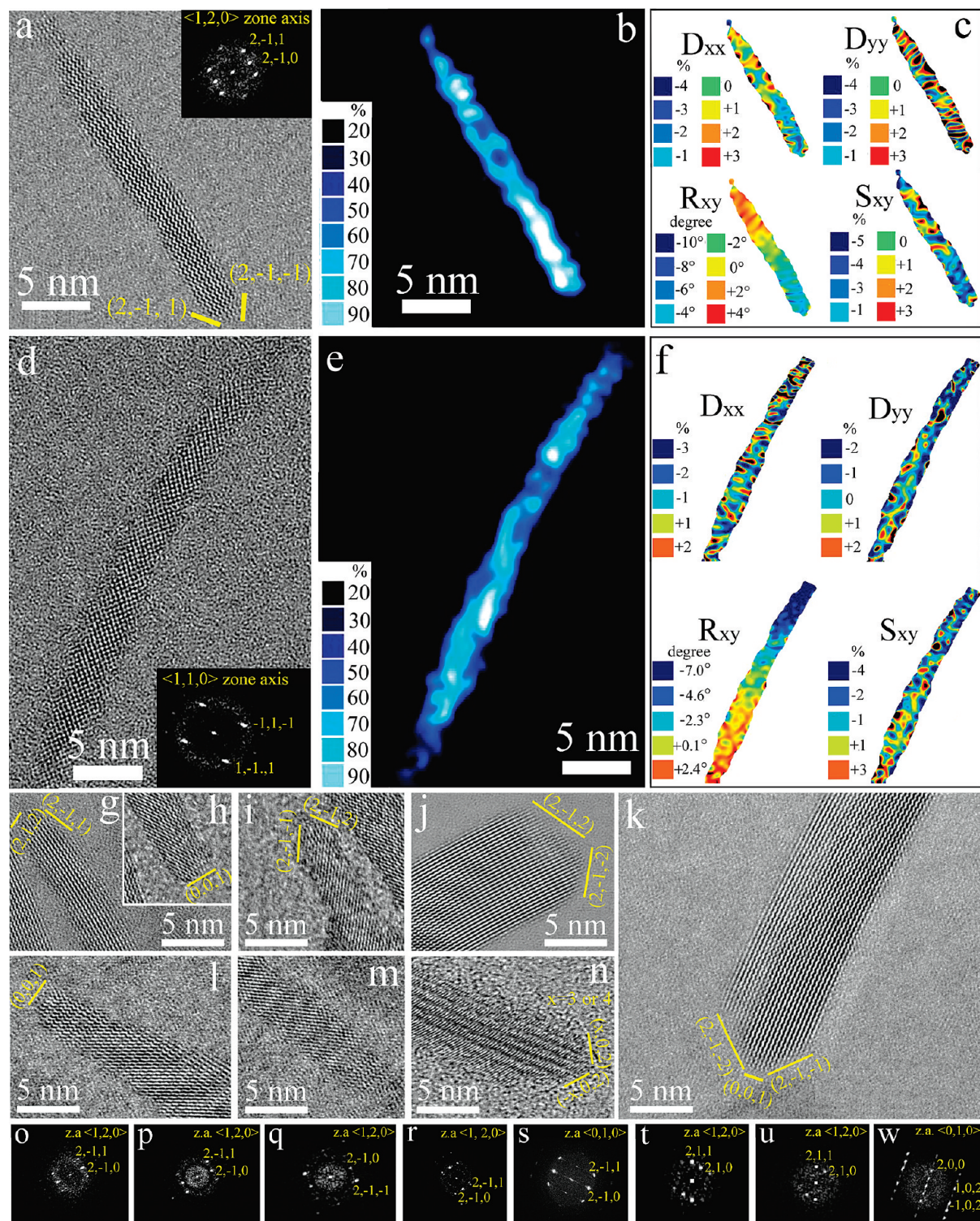
Figure 3. Phase-contrast HRTEM study of *b*-TiO$_2$ NR seeds: (a,d) Small-diameter NRs viewed along their $\langle 1,2,0 \rangle$ and $\langle 1,1,0 \rangle$ zone axis, respectively (the insets show the corresponding FFTs). (b,e) False-color crystal-phase amplitude maps obtained by HRTEM contrast analysis of the most intense fringes in the images in panels a and d, respectively. (c,f) False-color strain maps of fringe displacement in the direction perpendicular (D_{xx}) and parallel to the long nanorod axis (D_{yy}), of fringe rotation (R_{xy}), and of shear stress (S_{xy}), obtained by GPA analysis of the most prominent fringes in the HRTEM images in panels a and d, respectively. (g–n) Magnified HRTEM views of the apexes of differently sized NRs. (o–w) FFTs relative to the nanostructure sections shown in panels g–n, respectively.

centrosymmetry of the orthorhombic brookite unit cell structure[23b,34] (Figure S5 in the Supporting Information). The complex NR shaping mode verified experimentally can be better explained as arising from accentuation of anisotropic crystal development assisted by facet-preferential surfactant binding

under far-from-equilibrium growth conditions. Actually, according to the Mullins−Sekerka instability model,[34b,37] fast NC evolution in a diffusion-limited regime under intense monomer fluxes can involve a large probability of violent growth fluctuations in proximity of high-energy crystal sites (e.g., edges,

corners, asperities), which could lead, for instance, to imperfect atom addition or lattice restructuring, as well as to huge enhancement of crystal development rate thereon. Emergence of such kinetic instabilities can largely concur not only to promote arrow-like shaping via disappearance of the fastest-growing facets in favor of more stable lower-energy surfaces at the NR apexes, but also to drive the independent evolution of the latter, as observed for other systems.[1a,34]

3.2. Synthesis and Topological Control of HNCs. The high synthetic flexibility in the selection of *b*-TiO₂ NRs with tailored geometric features and peculiar surface faceting at the apexes transcribed into the availability of substrate seeds that could potentially exhibit anisotropic reactivity, that is, spatially dependent accessibility toward Fe$_x$O$_y$ deposition under suitable conditions. The results of the following sets of experiments illustrate how the seeding capabilities of the *b*-TiO₂ NRs were deduced through scrutinizing the impact of their geometric features as well of the reaction kinetics on the formation of *b*-TiO₂—Fe$_x$O$_y$ HNCs with programmable topologies.

Tip-Selective HNC Growth. Figure 4 demonstrates the degree of topological selectivity achieved by syntheses that combined the following conditions: (a) use of short-to-medium aspect-ratio *b*-TiO₂ NRs as seeds; and (b) addition of a fixed volume of rather concentrated Fe(CO)₅ solution (1 M) in the primary fast-injection step. The corresponding reaction details are summarized in Table 1. The TEM overview reveals the high-yield formation (>95%) of composite objects made of asymmetrically tipped rod-like sections, which exhibit a distinguishable image contrast variation across their profile. On the basis of the known decomposition pathways of Fe(CO)₅ in hot surfactant mixtures,[33] the obtained hybrid nanostructures could be preliminary interpreted as being individually constituted of a single nearly spherical head domain of Fe$_x$O$_y$ selectively attached to either terminations of one of the original TiO₂ NR seeds. This assignment was consistent with the comparatively higher average electron density expected for Fe$_x$O$_y$ relative to TiO₂. The formation of permanent *b*-TiO₂—Fe$_x$O$_y$ bonding junctions was supported by the fact that the relative heterostructure configuration could withstand repeated postsynthesis purification cycles and that, whenever necessary, the HNCs could be sorted out from unreacted TiO₂ seeds and/or independently nucleated Fe$_x$O$_y$ NCs upon careful nonsolvent destabilization combined with magnet attraction.

In line with earlier reports on other TiO₂—Fe$_x$O$_y$ systems,[19] monitoring of the reaction course confirmed that the heterostructures originated through direct deposition of Fe$_x$O$_y$ patches onto the TiO₂ seeds, followed by gradual enlargement of such domains over time, during which the percentage of heterostructures within the total particle population maintained invariant. Accordingly, as the seeds basically dictated the number of Fe$_x$O$_y$ nuclei generated, a reduction in the nominal NR content in the flask led to HNCs that carried proportionally larger Fe$_x$O$_y$ heads with sizes ranging from ∼4 to ∼10 nm (cf., Figure 4 and Table 1).

After the fast-injection step, slow controlled-rate supply of proportionally larger volumes of the secondary Fe(CO)₅:OLAC precursor feedstock solution afforded selective enlargement of the Fe$_x$O$_y$ head dimensions up to ∼40 nm, along which the projected heterostructure profile could accordingly vary from matchstick-type (Figure 4a−d) to mushroom-like (Figure 4e−g). It is notable that the one-sided Fe$_x$O$_y$ growth mode regime was safely maintained in seeded syntheses, which exploited similarly tapered NRs with diameter and length dimensions spanning size

intervals as wide as ∼3−10 nm and ∼25−70 nm, respectively. On the other hand, when the reactants were replenished by reiterating fast single-shot additions (even at sufficiently large time intervals in between consecutive injections), the samples could be detrimentally contaminated with independently generated Fe$_x$O$_y$ NCs. Remarkably, HNCs consisting of multiply Fe$_x$O$_y$-decorated NRs were never observed under all synthesis conditions. Overall, our results demonstrated that the programmed reactant delivery technique, consisting of coupling a primary fast injection with cautiously calibrated secondary additions, guaranteed that growth of the Fe$_x$O$_y$ domains initially implanted onto the NRs was strongly favored over both reiteration of heterogeneous nucleation events and parasitic homogeneous nucleation of free-standing Fe$_x$O$_y$ NCs in the bulk medium. It is also worth remarking that these trends reflected well the typical dynamics of hindered nucleation and autocatalytic growth, which distinguishes Fe$_x$O$_y$ formation by nonhydrolytic pathways.[33]

Nonselective Growth on Exceedingly Large Seeds. The Fe$_x$O$_y$ deposition mode entered a nonselective regime as the TiO₂ seeds far exceeded a certain size threshold. Heterostructure synthesis seeded with high aspect ratio tapered *b*-TiO₂ NRs with diameter/length beyond ∼8/80 nm still yielded heterodimer HNCs, for which Fe$_x$O$_y$ did not, however, show any localization preference (Figure 4h). Actually, the product comprised a mixture matchstick-shaped and various types of longitudinally decorated HNCs, as expected on a statistical basis from site-random Fe$_x$O$_y$ nucleation. By comparison, it is useful to recall that analogous TiO₂—Fe$_x$O$_y$ heterostructures with uncontrolled architectural configurations were instead obtained as the exclusively accessible product when the seeding was accomplished with other types of crystal-phase-tailored and/or shaped TiO₂ seeds, regardless of their size.[19]

Topology Manipulation by Precursor Injection Modulation. A deviation from the one-sided Fe$_x$O$_y$ arrangement on the *b*-TiO₂ seeds was obtained by manipulating the kinetics of Fe$_x$O$_y$ heterogeneous nucleation. Figure 5 illustrates the effect of progressively decreasing the Fe(CO)₅ concentration of the primary feedstock solution (from 1 to about 0.1 M) employed in the primary fast-injection step under standard matchstick-generating conditions at a fixed TiO₂ seed content. The corresponding reaction details are summarized in Table 2. Because of the increasingly restricted precursor supply, the nucleation onset was delayed and the Fe$_x$O$_y$ domains eventually incorporated in the resulting binary HNCs could grow to proportionally smaller sizes (cf., Figure 5a,b,d). Interestingly, a topological transition from a tip-selective to a fully nonspecific deposition regime[1c,d,19] was appreciable, while HNC yield maintained invariant. The progression toward the new growth mode manifested through a gradual change in the relative abundance of matchstick-like HNCs within the particle population in favor of other heterostructure geometries, whereby the Fe$_x$O$_y$ domains could be accommodated at any relative position along the longitudinal sidewalls of the respective NR sections (cf., Figure 5a,b,d). Such a trend implied that a reduction in the nominal precursor to seed molar ratio caused a proportionally reduced probability of Fe$_x$O$_y$ deposition at the NR extremities, being compensated for by a correspondingly higher degree of heterogeneous nucleation at other surface sites.

A statistical evaluation of the relevant TEM overviews indicated that Fe$_x$O$_y$ domain size distribution converted from a monomodal (Figure 5a) to a quasi-bimodal type for moderately low Fe(CO)₅ loadings (Figure 5b). In the bimodal samples, the
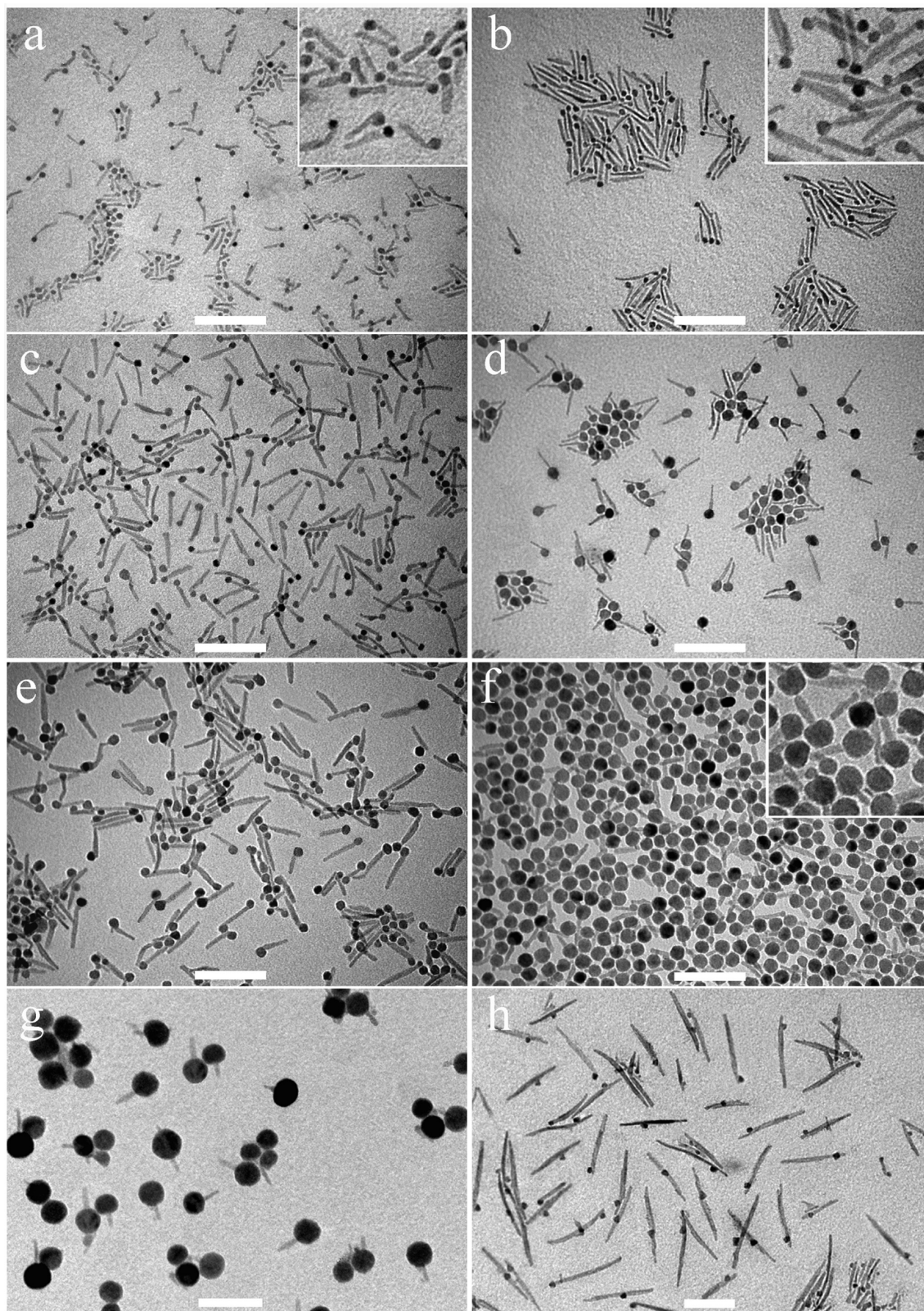
Figure 4. Representative low-magnification TEM overviews of (a−g) matchstick-shaped and (h) longitudinally decorated HNCs synthesized by reacting tapered *b*-TiO$_2$ NR seeds with different sizes and aspect ratios with varying amounts of Fe(CO)$_5$ in OLAC:OLAM:DDIOL:ODE mixtures (white scale bar = 100 nm). The relevant reaction parameters are summarized in Table 1.

larger Fe$_x$O$_y$ domains were mainly found on the apexes, while the smaller ones most frequently decorated the longitudinal sidewalls of the NRs. These findings suggested that these two HNC subfamilies were formed separately in time, with the

deposition at the NR tips occurring somewhat faster than at other seed sites. On the other side, a renewed convergence toward a monomodal type Fe$_x$O$_y$ size distribution was achieved upon excessive reduction of the Fe(CO)$_5$ amount added (Figure 5d),

Table 1. Reaction Parameters Used in the Synthesis of the HNCs Shown in Figure 4

	sample correspondence with images in Figure 4							
	panel a	panel b	panel c	panel d	panel e	panel f	panel g	panel h
TiO$_2$ seeds:								
short axis (nm)	3 ± 0.1	3 ± 0.1	5 ± 0.2	3 ± 0.1	7 ± 0.3	5 ± 0.2	5 ± 0.2	8 ± 0.5
long axis (nm)	20 ± 2	45 ± 3	60 ± 5	45 ± 3	60 ± 5	60 ± 5	60 ± 5	130 ± 10
TiO$_2$ in the flask (mmol)[a]	0.07	0.1	0.1	0.02	0.1	0.1	0.1	1
seed number × 10^{-9} (mmol)[b]	2.50	1.50	0.50	0.30	0.15	0.15	0.15	0.80
Fe(CO)$_5$ added by the primary fast injection (mmol)	1	1	1	1	1	1	1	1
Fe(CO)$_5$ added by the secondary slow injection (mmol)					2	6	10	

[a] Expressed as TiO$_2$ molecular units. [b] Expressed as number of TiO$_2$ NRs.

which accordingly reflected vanishing of the seed-site dependence of Fe$_x$O$_y$ heterogeneous nucleation rate otherwise observed at intermediate precursor loadings. Regardless of the HNC configurations initially attained, supplemental precursor feed-stock delivery subsequent to the primary fast-injection step allowed selective enlargement of the previously implanted Fe$_x$O$_y$ domains and promoted moderate focusing of their size distribution without altering the pristine distributions of the heterostructure topological arrangement (cf., Figure 5b,c,d–f).

To further clarify the mechanism underlying the topology switching, we examined the influence of altering other reaction parameters on the evolution of HNC configuration. In general, for fixed amount of Fe(CO)$_5$ injected, the progressive loss of the tip-preferential Fe$_x$O$_y$ deposition mode was found to be accentuated with increasing NR concentration in the flask. As opposed, at extremely low TiO$_2$ content, matchstick-like HNCs represented the dominant product, although the particle population could be contaminated by homogeneously nucleated Fe$_x$O$_y$ NCs to an extent that depended on the relative Fe(CO)$_5$ excess. On the other side, variations in the absolute surfactant content by a factor of ∼2 to ∼6 (as done for the precursor amount in the injection-modulated synthesis) at a fixed TiO$_2$/Fe(CO)$_5$ ratio did not impact on the expected synthesis outcome to any significant extent. Again, in no circumstances were multiply Fe$_x$O$_y$-decorated NRs formed.

While confirming the self-catalytic nature of Fe$_x$O$_y$ growth stage in our seeded environment,[33] all experimental proofs reported above suggest that the site-selective Fe$_x$O$_y$ deposition on the seed should be a process kinetically regulated by the reactive monomer flux that sets in after the primary fast precursor injection step, depending on the relative Fe(CO)$_5$ to b-TiO$_2$ proportions realized. On the other hand, it also appears clear that the mechanism underlying spatially controlled heterogeneous nucleation greatly profits from exploitation of specifically sized and shape-tapered b-TiO$_2$ NRs as seeds in order to operate effectively. The necessity of subtle structural prerequisites that the seed should meet to allow for topology selection is highlighted by the outcome of seeded-growth syntheses accomplished with other types of crystal-phase tailored and/or shaped TiO$_2$ NRs, from which TiO$_2$/Fe$_x$O$_y$ HNCs with random configurations could be exclusively obtained, regardless of the seed size and of precursor supply conditions.[19]

3.3. Structural Characterization of the HNCs. The representative SR-XRD pattern of matchstick-like HNCs made of 60 ± 4 nm b-TiO$_2$ NRs decorated with ∼10 ± 1 nm Fe$_x$O$_y$ heads in Figure 2 (trace b) exhibits a complex scenario of signals arising from the convoluted contributions of b-TiO$_2$ and Fe$_x$O$_y$ in the inverse spinel cubic structure of magnetite (Fe$_3$O$_4$) and/or maghemite (γ-Fe$_2$O$_3$). The two Fe$_x$O$_y$ polymorphs phases, authenticated by emergence of the prominent (220), (311), (400), (440), and (511) reflections, cannot be discriminated due to their

crystallographic similarity and the inherently large line widths leading to strong overlapping of several reflections. Accordingly, Rietveld-based fits[28] of the patterns were satisfactory accomplished regardless of whether the samples were assumed to be composed of b-TiO$_2$/γ-Fe$_2$O$_3$ or b-TiO$_2$/Fe$_3$O$_4$ phase mixtures. Interestingly, in addition to confirming retention of the TiO$_2$ brookite structure of the NR seeds in final HNC product, calculation of refined lattice parameters evidenced that the b-TiO$_2$ unit cell volume had undergone an average compression of about 1% following Fe$_x$O$_y$ deposition.

Phase-contrast HRTEM investigations provided detailed information on the structure of individual HNCs for different topological configurations. Various cases of b-TiO$_2$/Fe$_x$O$_y$ heterointerfaces were encountered, among which the most frequently observed are described in the following. Figure 6 reports representative HRTEM studies of matchstick-shaped HNCs (Figure 6a,g,o). In agreement with the SR-XRD data, the FFT calculations of the corresponding images (Figure 6b,c, h,i, p,q) confirmed that the HNCs individually embodied one of the original [0,0,1]-elongated orthorhombic b-TiO$_2$ seed in their rod-shaped tail section, while the spherical head located at one apex was a single-crystalline Fe$_x$O$_y$ domain in the inverse spinel cubic phases of indistinguishable Fe$_3$O$_4$/γ-Fe$_2$O$_3$.[19,33] The FFT patterns of the two lattices were merged to determine the crystallographic relationships holding between them in the respective cases. The joint diffractograms (Figure 6d,l,r) clarify that distinct HNCs embody the two materials arranged in nonequivalent relative configurations. On a first approximation, the two domains were assumed to be separated by continuous sharp heterointerfaces (marked by yellow dotted lines in panels e,m,s). The latter were inferred to be almost or fully parallel to those sets of b-TiO$_2$ facets that have been identified at the apexes of the starting seeds (cf., Figure 3). For example, for the specific cases addressed in Figure 6, the orientations of the boundary junctions actually coincide to those of the (0,0,1)$_{TiO_2}$, (2,−2,−1)$_{TiO_2}$, and (1,−1,−1)$_{TiO_2}$ planes, respectively, which accordingly indicates Fe$_x$O$_y$ preference to nucleate and grow thereon.

The conditions of planar epitaxy subsisting between the b-TiO$_2$ and Fe$_x$O$_y$ lattices were determined and expressed in terms of interfacial atomic plane continuity, according to the Coincidence Site Lattice theory (CSLT).[39,40] The CSLT is used to explain the crystallographic relationships between two types of materials by identifying the degree of matching between points of the respective lattices, and the frequency at which this correspondence occurs along the relevant grain boundaries.[1,3,15,19a,39]

(39) Randle, V. *The Role of the Coincidence Site Lattice in Grain Boundary Engineering*; Woodhead Publishing Limited: Cambridge, England, 1997.
(40) Markov, I. V. *Crystal Growth for Beginners: Fundamentals of Nucleation, Crystal Growth, and Epitaxy*; World Scientific: Singapore, 2003.
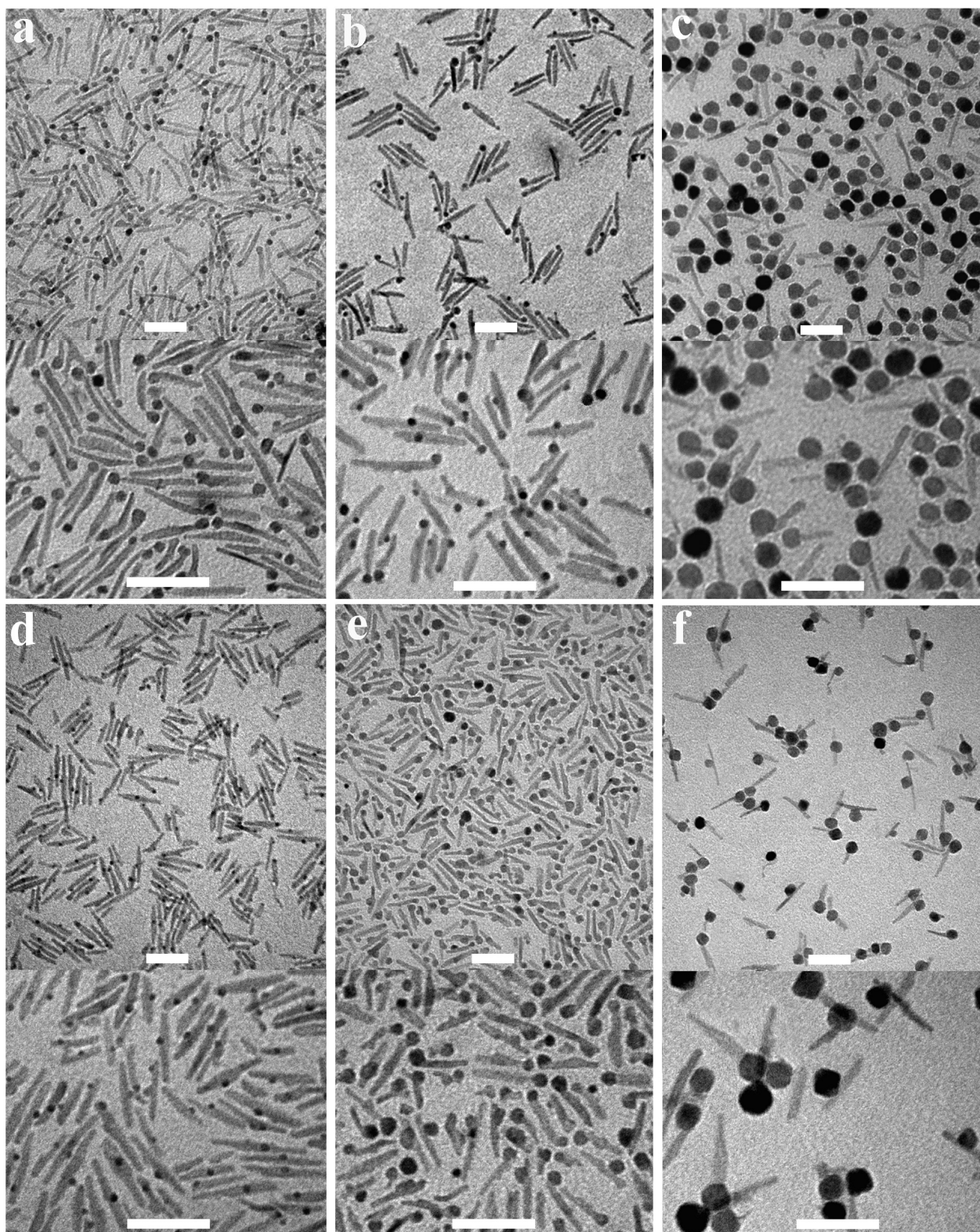
Figure 5. Representative low-magnification TEM images of HNCs achieved in precursor-injection-modulated experiments: (a,b,d) HNCs obtained from the same NR seeds upon adding progressively lower Fe(CO)$_5$ amounts in the fast-injection step; (c,e,f) HNCs deriving from the heterostructures shown in panels b and d, respectively, after slow supply of extra precursor feedstock solution (the white scale bar = 50 nm). The relevant reaction conditions are summarized in Table 2.

For example, the b-TiO$_2$ and Fe$_x$O$_y$ domains of the matchstick HNC in Figure 6a,e are oriented such that a steady correspondence exists between the $(-1,3,1)_{Fe_xO_y}$ spacings and the projections of the $(2,-2,-1)_{TiO_2}$ planes on the recognizable one-

dimensional heterointerface. Analogously, for the heterostructures reported in panels g, m and panels o, s, the projections of the $(3,1,1)_{Fe_xO_y}$ and $(2,2,0)_{Fe_xO_y}$ planes coincide regularly with those of the $(-1,1,-1)_{TiO_2}$ or the $(3,3,1)_{TiO_2}$ planes, on the

Table 2. Reaction Parameters Used in the Synthesis of the HNCs Shown in Figure 5

	sample correspondence with images in Figure 5					
	panel a	panel b	panel c	panel d	panel e	panel f
TiO₂ seeds:						
short axis (nm)	4	4	4	4	4	4
long axis (nm)	60	60	60	60	60	60
TiO₂ in the flask (mmol)[a]	0.1	0.1	0.1	0.1	0.1	0.1
seed number × 10^{-9} (mmol)[b]	0.5	0.5	0.5	0.5	0.5	0.5
Fe(CO)₅ added by the primary fast injection (mmol)	1	0.5	0.5	0.1	0.1	0.1
Fe(CO)₅ added by the secondary slow injection (mmol)			4		2	5

[a] Expressed as TiO₂ molecular units. [b] Expressed as average number of TiO₂ NRs.

respective heterointerfaces. The interfacial lattice misfit associated with the aforementioned heterostructure configurations can be calculated to be of about +7%, +4%, and −6%, where the signs "+" and "−" denote the direction of the deformation (i.e., expansion or contraction, respectively), which the b-TiO₂ structure should undergo to achieve perfect coincidence site lattice correspondence with Fe$_x$O$_y$.

For the sake of a comparative structural evaluation, HRTEM investigations were also performed on HNCs made of longitudinally Fe$_x$O$_y$-decorated b-TiO₂ NRs. Representative results are reported in Figure 7. Here, the relative orientation of the heterointerfaces was always found to be parallel to the c-axis of the NR seeds, which substantiated preservation of the seed structure along the process of Fe$_x$O$_y$ overgrowth. Under the most commonly observed zone axes, the expression of epitaxial relationships on the basis of the CSLT argument evidenced a generally better lattice matching for these nonselective heterostructure configurations. For example, for the two HNCs illustrated in Figure 7, the interfacial projections of the $(1,-1,-1)_{TiO_2}$ planes (Figure 7a,e) and of the $(0,0,2)_{TiO_2}$ planes (Figure 7g,m) correspond regularly to those of the $(-1,3,1)_{Fe_xO_y}$ and $(1,3,1)_{Fe_xO_y}$ planes, respectively. The deducible mismatch is of about 0.2% and 1.5% for the respective cases. Interestingly, we performed atomistic modeling[15] of the interface structure examined down different orientations, which revealed that the coherent attachment between the b-TiO₂ and Fe$_x$O$_y$ domains could be attained at the cost of a much higher lattice mismatch along zone axes other than those captured experimentally. For example, the alternative heterostructure view offered by the model constructed for the HNC in Figure 7a−f, following a 90° rotation around to the junction plane, demonstrates a misfit as high as ∼7% along the new visible interface (Figure S6 in the Supporting Information). In general, as the actual b-TiO₂/Fe$_x$O$_y$ junction is built-up three-dimensionally, it is likely to involve different degrees of lattice matching, depending on the heterostructure orientation under which the relevant interface is concerned. This fact suggests that the overall misfit strain energy accumulated in the longitudinally Fe$_x$O$_y$-functionalized NRs may not diverge exceedingly from that tolerated by the asymmetrically Fe$_x$O$_y$-tipped NRs. Analogous deductions were previously reported for other prototypes of topologically selectable TiO₂-based heterostructures.[15]

To better elucidate the bonding relationships and strain distribution in the heterostructures, changes in HRTEM contrast amplitude and fringe displacement across the HNCs were analyzed in detail, as previously done for the starting NR seeds (cf., Figure 3).

The spatial localization of b-TiO₂ and Fe$_x$O$_y$ phase components within the heterostructures was first assessed by analyzing the local HRTEM contrast amplitude of periodicities distinctive of each crystal phase.[19a,29,35] The as-derived crystal-phase maps

disclosed the detailed topological distribution of the b-TiO₂ and spinel cubic Fe$_x$O$_y$ components in the tail and head sections, respectively, which confirmed preservation of the size and shape of the seeds during Fe$_x$O$_y$ deposition on their arrow-shaped terminations. The relative extent of fringe visibility attenuation recognizable along the b-TiO₂ portion resembles that indentified for the bare NRs as a consequence of their intrinsic bending (cf., Figure 3). This fact indicates that Fe$_x$O$_y$ overgrowth had not significantly altered the natural curvature of the seeds, as expected on the basis of the limited surface fraction occupied by the joint Fe$_x$O$_y$ domains. On the other side, although a relatively more uniform HRTEM contrast generally characterizes the Fe$_x$O$_y$ sections, the latter occasionally present an abrupt amplitude decrease over limited areas (Figure 6s,t and Figure 7a−f). Such fringe intensity changes may not necessarily be related to lattice distortion consequent to heterojunction formation. In fact, similar effects were also encountered in isolate Fe$_x$O$_y$ NCs, whereby they could be ascribed to local alteration in the dynamical electron diffraction condition due, for instance, to a local tilt and/or variation in nanocrystal thickness.

The crystal-phase maps clarify that that the two domains actually shared interfaces of variable extensions, depending on whether the Fe$_x$O$_y$ head was narrowly accommodated either on the small basal (001)-type sides (Figure 6f), on the more developed higher-index oblique facets at the apex sections (Figure 6n,t), or on the longitudinal sidewalls (Figure 7f,n). This is qualitatively consistent with the extent of interfacial strain experienced by the two materials in the respective cases, according to which proportionally smaller contact areas corresponded to higher degrees of lattice mismatch at the relevant junctions. Here, it should, however, be noted that the apparent irregularities that characterize the interface boundaries, such as local abrupt change in their running directions or extended curvature, are topologically meaningless, because they are affected by fringe delocalization effects and strongly depend on the defocus value at which the experimental images are recorded (as demonstrated by pertinent HRTEM simulations in Figure S7 of the Supporting Information).

The application of the GPA approach[19,29−31] to probe lattice fringe displacement and rotation provided interesting information on the evolution of strain in the b-TiO₂ NRs following heterostructure formation. The representative GPA analyses of matchstick-like and longitudinally functionalized HNCs addressed in Figure 6u and Figure 7o, respectively, suggest some major differences in strain component distribution, as compared to those found for the bare NRs. On one side, the R_{xy} maps confirm a steady lattice fringe rotation along the NR section, which is ascribable to the obvious nanostructure curvature. On the other side, the D_{yy} map highlights emergence of significant b-TiO₂ lattice deformation in proximity to the attached Fe$_x$O$_y$ domain. In particular, the fringes running orthogonal to the
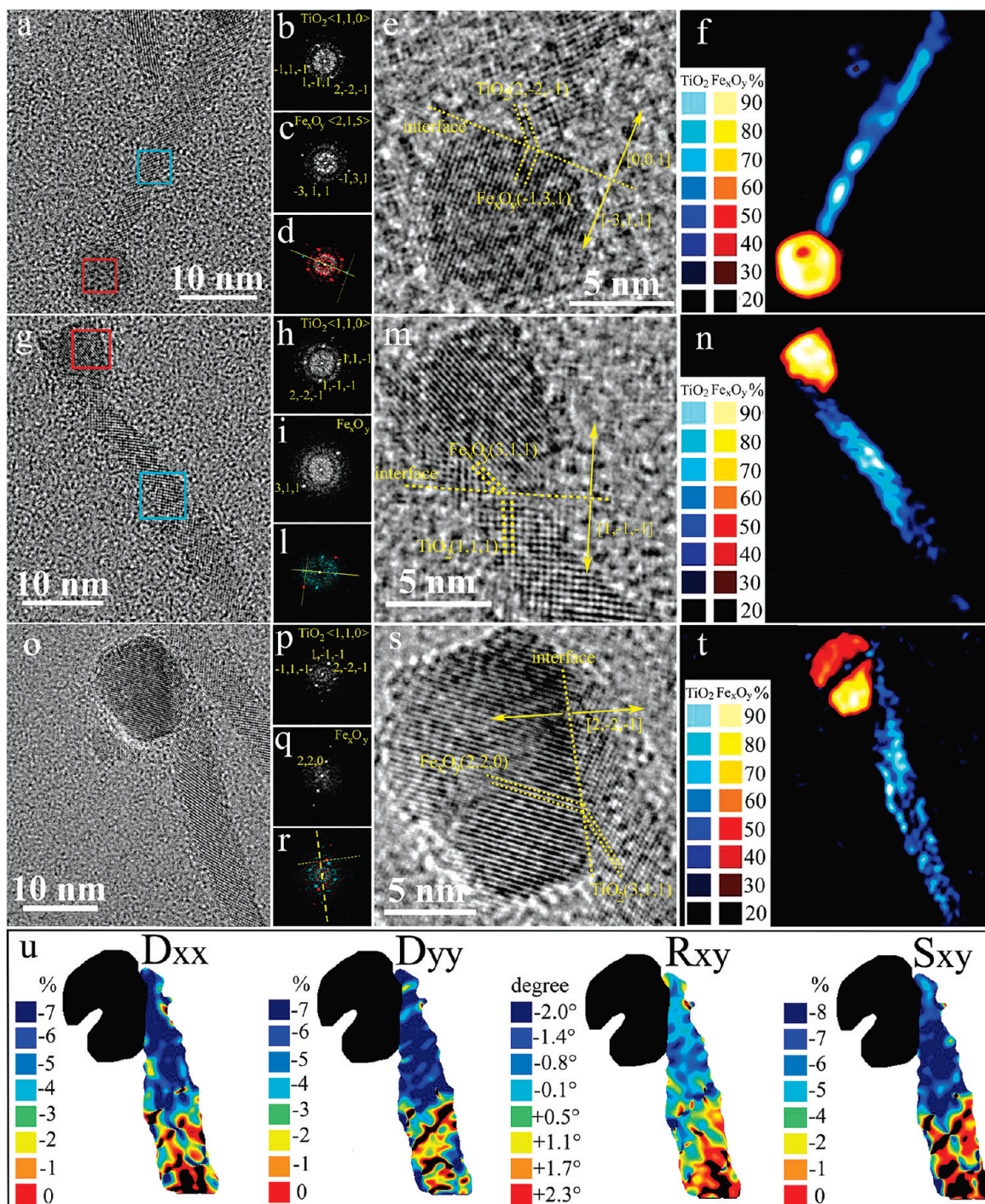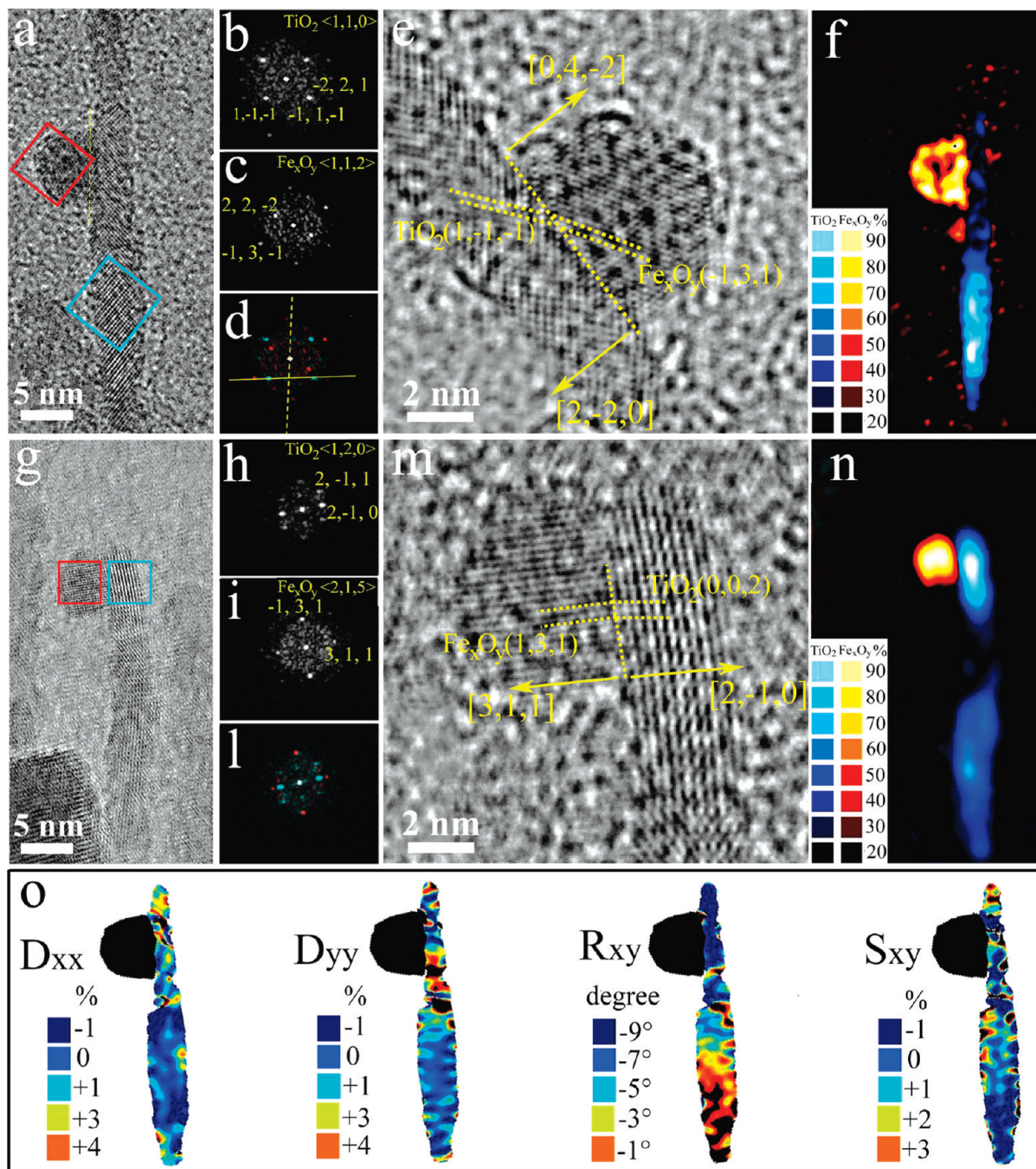
Figure 6. Phase-contrast HRTEM study of HNCs made of asymmetrically Fe_xO_y-tipped TiO_2 nanorods. (a,g,o) HRTEM images of matchstick-like HNCs that incorporate TiO_2 and Fe_xO_y in different relative arrangements. (b,c,h,i,p,q) FFTs calculated from the regions enclosed by the blue and the red boxes in panels a, g, and o, respectively. Brookite TiO_2 is viewed along the $\langle 1,1,0\rangle$ zone axis in all cases, while a univocal $\langle 2,1,5\rangle$ zone axis can be assigned to inverse spinel cubic Fe_xO_y only for the case in panels a and c. (d,l,r) Joint diffractograms obtained by merging the FFTs in panels b,c, h,i, and p,q, respectively, each traced by a different color. (e,m,s) Magnified views of the matchstick head regions corresponding to the heterostructures in panels a, g, and o, respectively. The relative orientations of the interfacial planes between the two material domains, deduced from the FFT analyses, are marked by dotted yellow lines that correspond to the interface projections in the respective image planes. In panel e, the interface is perpendicular to the $[0,0,1]_{TiO_2}$ and the $[-3,1,1]_{Fe_xO_y}$ directions, while in panels m and s the interface is perpendicular to the $[1,-1,-1]_{TiO_2}$ and $[2,-2,-1]_{TiO_2}$ directions, respectively. The epitaxial relationships between the two lattices are indicated. The interfacial lattice mismatch on the visible one-dimensional projected interfaces can be calculated as:

$$(d^{Fe_xO_y}_{(-1,3,1)} - d^{TiO_2}_{(2,-2,1)}\cos(25°))/(d^{TiO_2}_{(2,-2,1)}\cos(25°)) = +7\%; (d^{Fe_xO_y}_{(3,1,1)}/\cos(45°) - d^{TiO_2}_{(1,1,1)})/(d^{TiO_2}_{(1,1,1)}) = +4\%$$
$$(d^{Fe_xO_y}_{(2,2,0)}/\cos(27°) - d^{TiO_2}_{(3,3,1)}/\cos(65°))/(d^{TiO_2}_{(3,3,1)}/\cos(65°)) = -6\% \text{ for the respective cases}$$

(f,n,t) False-color crystal-phase amplitude maps obtained by HRTEM contrast analysis of the images in panels a, g, and o, respectively. The blue and red colors are related to the most intense fringes of the TiO_2 and Fe_xO_y lattices, respectively, as indicated in the legends. Note that the black regions identifiable in the middle of the Fe_xO_y domains in panels f and t correspond to an effective reduction of the fringe visibility thereon, possibly due to local variation of the dynamical diffraction condition. (u) False-color strain maps of fringe displacement in the direction perpendicular (D_{xx}) or parallel to the long NR axis (D_{yy}), of fringe rotation (R_{xy}), and of shear stress (S_{xy}) for the rod-like sections of the HNCs, obtained by GPA analyses of the most prominent b-TiO_2 lattice fringes visible in the HRTEM image in panel o.

Figure 7. Phase-contrast HRTEM study of HNCs made of TiO₂ nanorods decorated with Fe$_x$O$_y$ domains on their longitudinal sidewalls: (a,g) HRTEM images of heterostructures in different relative configurations. (b,c,h,i) Corresponding fast Fourier transform (FFT) analyses of the regions enclosed by the blue and the red boxes in panel a, which correspond to brookite TiO₂ viewed along the ⟨1,1,0⟩ and ⟨1,2,0⟩ zone axis, and inverse spinel cubic Fe$_x$O$_y$ down the ⟨1,1,2⟩ and ⟨2,1,5⟩ zone axis, respectively. (d,l) Joint diffractograms obtained by merging the FFTs in panels b,c and h,i, respectively, each traced by a different color. (e,m) Magnified HRTEM view of the matchstick head in panels a,g. The relative orientations of the interfacial planes between the two material domains are marked by dotted yellow lines. In panel e, the interface is perpendicular to the $[2,-2,0]_{TiO_2}$ and $[0,4,-2]_{Fe_xO_y}$ directions, while in panel m the interface is approximately perpendicular to the $[2,-1,0]_{TiO_2}$ and $[3,1,1]_{Fe_xO_y}$ directions, respectively. The lattice mismatch can be calculated as:

$$(d^{Fe_xO_y}_{(-1,3,1)}/\cos(60°) - d^{TiO_2}_{(1,-1,-1)}/\cos(47°))/(d^{TiO_2}_{(1,-1,-1)}/\cos(47°)) = -0.2\% \quad (d^{Fe_xO_y}_{(1,3,1)} - d^{TiO_2}_{(0,0,2)})/(d^{TiO_2}_{(0,0,2)}) = -1.5\% \text{ for the respective cases}$$

(f,n) False-color crystal-phase amplitude maps obtained by HRTEM contrast analysis of the images in panels a,g, respectively: the blue and red colors are related to the most intense fringes of the TiO₂ and Fe$_x$O$_y$ lattices, respectively, as indicated in the legends. Note that the black regions identifiable in the middle of the Fe$_x$O$_y$ domains (red) in panel f correspond to an effective reduction of the fringe visibility thereon, possibly due to local variation in the dynamical diffraction condition. The disappearance of the TiO₂ fringes in panels f,n is due to a rotation of the rod lattice. (o) False-color strain maps of fringe displacement in the direction perpendicular (D_{xx}) or parallel to the long NR axis (D_{yy}), of fringe rotation (R_{xy}), and of shear stress (S_{xy}) for the rod-like sections of the HNCs, obtained by GPA analyses of the HRTEM image in panel a.

c-axis exhibit a sudden spacing contraction of 7−8% (Figure 6u) or expansion of ∼4−5% (Figure 7o) as they approach and span a NR portion that extends a few square nanometers far ahead of the area shadowed by the Fe$_x$O$_y$ domain. Across the

deformed NR region, being approximately twice as extended as the seed area in front of Fe$_x$O$_y$, the degree of strain maintains approximately constant, while it steeply declines elsewhere (see the corresponding strain profiles in Figure S8 of the Supporting

Information). Within the limits of our HRTEM investigations (~50 objects examined for each topology), the strain signature appeared to be more pronounced for the matchstick HNCs (7−8%, Figure 6u) than for their longitudinally decorated counterpart (4−5%, Figure 7o). In this respect, it is worth stressing that HRTEM and SR-XRD do not provide contradictory results regarding the extent of lattice strain in the HNCs. Indeed, the GPA treatment of HRTEM images decoupled strain in individual heterostructures, where lattice deformation was spatially confined to a fraction (20−40%) of the overall NR domain volume. Differently, the SR-XRD data embodied structural information collected on a highly statistically meaningful basis, the analysis of which provided an estimation of average strain degree, which was consistently much lower (~1%) than the one derived from GPA-HRTEM.

As for what regards the HNC in Figure 7o, some additional aspects deserve remark. For example, it can be noticed that the maximum percentage degree of strain inferred in Figure 7o (cf., D_{xx} and D_{yy} maps) largely fails to approach the interfacial lattice mismatch value deduced on the basis of the CSLT, which has been in fact estimated to be almost negligible (0.1%, cf., Figure 7e and o). This discrepancy can be explained by considering that the CSLT treatment provides a measure of the in-plane lattice fit by evaluating the interfacial correspondence of the atomic plane spacings of the corresponding bulk materials for the particular heterostructure geometry concerned. Thus, CSLT-estimated misfit describes a deformation that develops only across the plane on which the heterostructure lies.[39,40] Differently, the topological variation of lattice strain in the GPA map can be expected to reflect, although indirectly, extra deformation effects induced by highly detrimental interfacial lattice mismatch conditions holding along other out-of-plane crystallographic directions. Our interface structure models indeed confirmed that such circumstances actually subsisted for the HNC studied in Figure 7a−f (Figure S6 in the Supporting Information).

Additional interesting structural details can be inferred on comparing the D_{xx} and D_{yy} maps in Figure 7o. It emerges that the deformation developing in the *y* direction, that is, along the *c*-axis of the NR section, is comparatively much higher than the one developing along the perpendicular *x* direction. Furthermore, it can be appreciated that the strain signature appears to be especially concentrated at the edges of the interface while propagating far beyond. Simplified finite-element calculations of the elastic response of a TiO_2 NR joint to Fe_xO_y particle supported the hypothesis that the features highlighted above could possibly originate from the inherent anisotropic deformability of the orthorhombic *b*-TiO_2 lattice (Figure S9 in the Supporting Information), as suggested by recent mechanical studies.[41]

In all cases investigated by us, the general observation that the lattice fringe displacement involves a relatively large portion of the *b*-TiO_2 seed, which extends far beyond the *b*-TiO_2/Fe_xO_y junction region, while being attenuated only at a significant distance from it, points out that the *b*-TiO_2/Fe_xO_y interfacial mismatch should be the main source of lattice strain in these heterostructures. The absence of interface dislocations suggests
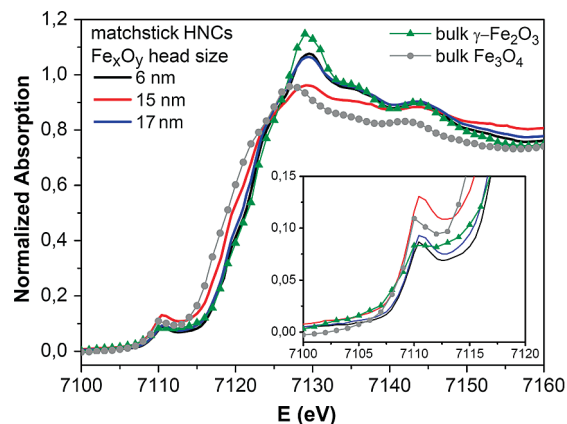
Figure 8. Normalized XANES spectra of matchstick-like HNCs made of ~5 × 50 nm *b*-TiO_2 sections tipped with Fe_xO_y heads of ~6, ~15, and ~17 nm, respectively, along with the spectra of bulk γ-Fe_2O_3 and Fe_3O_4 references. The inset shows a magnified view of the pre-edge peak region.

operation of mechanisms of strain propagation proceeding through long-range elastic transmission rather than via plastic relaxation.[40]

3.4. Iron Oxide Phase Composition. XANES measurements were performed to examine the average oxidation state of Fe in the samples and, hence, to discriminate between Fe_3O_4 and γ-Fe_2O_3 phases. Figure 8 displays the XANES spectra at the Fe *K*-edge of matchstick-shaped HNCs made of ~5 nm × ~60 nm *b*-TiO_2 NRs tipped with Fe_xO_y domains of ~6, ~15, and ~17 nm, respectively. XANES at the *K*-edge of transition metals in oxides originates from the excitation of a 1s photoelectron into p-type states. A pre-edge peak may occur due to 1s to 3d transitions with 3d−4p mixing, which involve cations in noncentrosymmetric positions.[42,43a] In the case of spinel Fe_xO_y (γ-Fe_2O_3 and Fe_3O_4), a prominent pre-edge peak, located at around 7110 eV, correlates with Fe cations in octahedral positions. Therefore, judging from the characteristic pre-edge features and their relative intensity with respect to the white line in Figure 8, the HNC samples can be concluded to contain spinel Fe_xO_y, in agreement with SR-XRD measurements. The presence of other minority phases, such as rhombohedral γ-Fe_2O_3 (hematite) and FeO (wüstite), can be safely ruled out, because the 1s to 3d transitions are known to be very weak for the former and forbidden for the latter.[42,43a] In addition, it can be noted that the spectra of the HNCs tipped with the ~6 and ~17 nm are very similar, while significantly differing from the spectrum of the heterostructures functionalized with ~15 nm Fe_xO_y heads, which in fact exhibits an absorption edge shifted by about 2 eV toward lower energies, a white line with reduced amplitude and sharpness, a shoulder at 7145 eV, and a more intense pre-edge peak. By comparison with the "fingerprints" of the reference compounds, the spectral details suggest that the former two samples should be in a more oxidized state closer

(41) (a) Krivtsov, A. M.; Morozov, N. F. *Phys. Solid State* **2002**, *44*, 2260–2265. (b) Park, S.-w.; Jang, J.-t.; Cheon, J.; Lee, H.-H.; Lee, D. R.; Lee, Y. *J. Phys. Chem. C* **2008**, *112*, 9627–9631. (c) Shokuhfar, T.; Arumugam, G. K.; Heiden, P. A.; Yassar, R. S.; Friedrich, C. *ACS Nano* **2009**, *3*, 3098–3102. (d) Crawford, G. A.; Chawla, N.; Das, K.; Bose, S.; Bandyopadhyay, A. *Acta Biomater.* **2007**, *3*, 359–367.
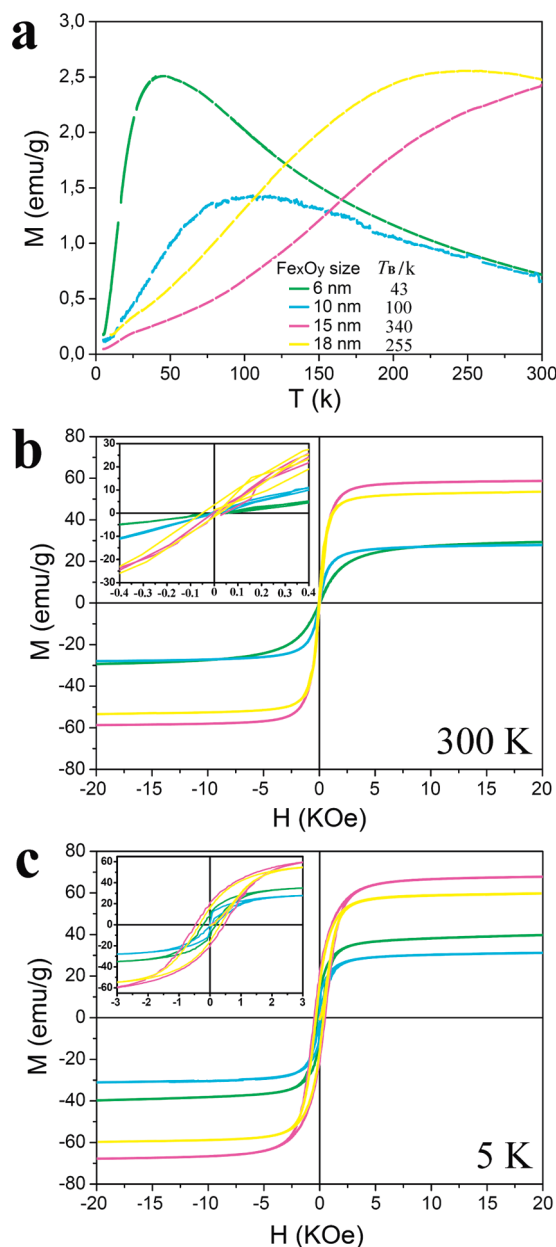
(42) (a) Grunes, L. A. *Phys. Rev. B* **1983**, *27*, 2111. (b) Corrias, A.; Mountjoy, G.; Loche, D.; Puntes, V.; Falqui, A.; Zanella, M.; Parak, W. J.; Casula, M. F. *J. Phys. Chem. C* **2009**, *113*, 18667–18675. (c) Lelis, M. F. F.; Porto, A. O.; Gonçalves, C. M.; Fabris, J. D. *J. Magn. Magn. Mater.* **2004**, *278*, 263–269. (d) Wilke, M.; Farges, F.; Petit, P. E.; Brown, G. E.; Martin, F. *Am. Mineral.* **2001**, *86*, 714–730.

(43) (a) Chen, L. X.; Liu, T.; Thurnauer, M. C.; Csencsits, R.; Rajh, T. *J. Phys. Chem. B* **2002**, *106*, 8539–8546. (b) Arcon, I.; Mozetic, M.; Kodre, A. *Vacuum* **2005**, *80*, 178–183. (c) Ichikuni, N.; Wakai, Y.; Hara, T.; Shimazu, S. *J. Phys. Conf. Ser.* **2009**, *190*, 012169.

to that of γ-Fe$_2$O$_3$, while both Fe$_3$O$_4$ and γ-Fe$_2$O$_3$ phases should coexist in the latter.[42,43]

The relative Fe$_3$O$_4$ to γ-Fe$_2$O$_3$ fractions were estimated by fitting the sample spectra to a weighted sum of the spectra of the corresponding bulk material references (note that this approach is limited by the fact XANES profiles of nanoscale samples can severely diverge from those of their bulk counterparts due to surface effects;[43a] therefore, the phase percentage estimations cannot be more accurate than ±5−8%). The relative γ-Fe$_2$O$_3$:Fe$_3$O$_4$ content was derived to be of about 80%:20% for the HNCs tipped with ∼6 and ∼17 nm Fe$_x$O$_y$ domains, and of 30%:70% for HNCs beating ∼15 nm Fe$_x$O$_y$ heads, respectively. According to previous Mössbauer spectroscopy investigations, Fe$_x$O$_y$ domains smaller than ∼11 nm grown on anatase TiO$_2$ NRs by an analogous nonhydrolytic route were also found to consist mainly of γ-Fe$_2$O$_3$.[19a] The nonmonotonic size-dependence of the spinel phase composition found here is not unexpected, given that the mechanisms leading to Fe$_x$O$_y$ formation depend not only on the specific chemical route exploited, but also on the structural quality of the Fe$_x$O$_y$ NCs that are eventually subjected to oxidation, as well as on the particular oxidant species eventually involved.[33,42b]

3.5. Magnetic Characterization. SQUID magnetometry was used to investigate the magnetic properties associated with the Fe$_x$O$_y$ component of the nanoheterostructures. Figure 9 summarizes the characterization results for various samples of matchstick-shaped HNCs grown from the same b-TiO$_2$ NRs (∼5 nm/∼50 nm) and carrying Fe$_x$O$_y$ domains with average sizes of about 6.1 ± 1.2, 8.1 ± 1.2, 9.9 ± 1.3, 15.6 ± 1.9, and 17.0 ± 2.3 nm (note that the diamagnetic contribution of TiO$_2$, measured independently, was negligible). The temperature-dependent magnetization (M) curves recorded after zero-field cooling (ZFC) were generally rather large, tending to broaden with increasing Fe$_x$O$_y$ head size (Figure 9a). The ZFC maxima, corresponding to the average blocking temperature (T_B), exhibited a general tendency to increase with the Fe$_x$O$_y$ size. In particular, the T_B values lay in between 40 and 150 K for Fe$_x$O$_y$ domains smaller than ∼10 nm, whereas they abruptly jumped to above 250 K for HNCs carrying Fe$_x$O$_y$ domains larger than ∼12−15 nm. Minor deviations from this behavior were found for samples of HNCs bearing Fe$_x$O$_y$ with nominally similar sizes, which preliminarily suggested that the size-dependence of T_B could be additionally modulated by the existence of b-TiO$_2$/Fe$_x$O$_y$ bonding interfaces with different structure and extension. This hypothesis was further corroborated by the observation that HNCs generally exhibited a sharper temperature-dependence of M, hence a narrower distribution of energy barrier for M reversal, relative to their NR/Fe$_x$O$_y$ NC physical mixture counterparts. The latter exhibited a behavior resembling that of pure Fe$_x$O$_y$ NCs[33b,c,42b,44] (Figure S10 in the Supporting Information).

The field-dependence of the magnetization coherently confirmed the ZFC data. Indeed, the magnetization curves recorded at room temperature (Figure 9b) for HNCs equipped with smaller Fe$_x$O$_y$ heads (below ∼10 nm) followed the Langevin function, authenticating a superparamagnetic behavior. On the contrary, the magnetization curves of HNCs carrying much larger Fe$_x$O$_y$ domains exhibited coercive fields, H_C, of the order

(44) (a) Kachkachi, H.; Ezzir, A.; Nogues, M.; Tronc, E. *Eur. Phys. J. B* **2000**, *14*, 681−689. (b) Battle, X.; Labarta, A. *J. Phys. D: Appl. Phys.* **2002**, *35*, R15−R42.

Figure 9. Magnetic characterization of matchstick-like HNCs grown from 4−5 × 50 nm sized b-TiO$_2$ NR seeds and tipped with Fe$_x$O$_y$ heads of 6.1 ± 1.2, 8.1 ± 1.2, 9.9 ± 1.3, 15.6 ± 1.9, and 17.0 ± 2.3 nm, respectively. (a) Temperature-dependent ZFC magnetization curves. (b,c) Field-dependent magnetization curves recorded at 300 and 5 K, respectively. The insets in panels b and c are expanded views of the respective low-field regions.

of 20−40 Oe and remanence, M_R, of about 1 emu/g, demonstrating that a fraction of the HNCs was blocked already at room temperature.

At 5 K (Figure 9c), the samples still displayed symmetric single-loop cycles with M reaching saturation even at moderate fields, which implied the absence of any appreciable fraction of a decoupled surface spinglass-like surface phase with higher magnetic anisotropy.[33b,c,42b,44] The saturation magnetization, M_S, values were rather spread (39.7 ± 0.5, 72.0 ± 0.5, 31.2 ± 0.5, 67.8 ± 0.5, and 59.2 ± 0.5 emu/g for HNCs tipped with increasingly larger Fe$_x$O$_y$ heads, respectively), all falling below the values expected for bulk γ-Fe$_2$O$_3$ (90 emu/g) and Fe$_3$O$_4$ (80−84 emu/g). It is known that such M_S reduction in nanoscale spinel ferrite material manifests magnetic disorder due to the

concurrence of various surface effects, among which a major role is played by canted and/or disordered spins associated with coordinatively unsaturated surface atoms, broken exchange bonds, and surface strain (the diamagnetic contribution of the bound surfactants can be safely considered insignificant).[33b−d,42b,44] Notably, the M_S values associated with the HNCs and their b-TiO$_2$/Fe$_x$O$_y$ physical mixture counterpart were 60−65% and 15−20% lower than M_S measured for corresponding pure Fe$_x$O$_y$ NCs, respectively (Figure S10 in the Supporting Information). This evidence pointed to the existence of extra demagnetization effects related to the b-TiO$_2$/Fe$_x$O$_y$ interfaces in the HNCs, which could not be otherwise accounted for by changes in dipolar coupling[1c,15] or interfacial chemical reactions.[59] Analogous to the M_S behavior, the H_C values at 5 K oscillated over a rather broad range (210 ± 15, 80 ± 15, 50 ± 15, 490 ± 15, and 330 ± 15 Oe, respectively), which could not be traced to any clear size-dependent trend, as opposed to what has generally been observed for isolated Fe$_x$O$_y$ NCs.[33b−d,42b,44]

3.6. Photocatalytic Properties. We examined the photocatalytic properties of our coupled semiconductor heterostructures with type-I band staggering, with respect to their ability to accumulate electrons under continuous UV irradiation at 365 nm and/or utilize stored charges for subsequent dark reactions. As a representative case of study, a comparative solution-phase examination of the behavior of b-TiO$_2$ NRs (with diameter/ length of ∼5 nm/∼50 nm) with respect to those exhibited by HNCs derived thereof (tipped with ∼10 nm Fe$_x$O$_y$ heads) and by corresponding NR/Fe$_x$O$_y$ NC physical mixtures is reported in Figures 10 and 11. The pertinent energy diagram, constructed on the basis of the band gaps of the respective bulk materials (0.1, 2.3, and 3.4 eV for half-metallic Fe$_3$O$_4$, γ-Fe$_2$O$_3$, and b-TiO$_2$, respectively), and the relevant photocatalytic processes are sketched in Scheme 1. The experiments were carried out in O$_2$-free anhydrous organic solvents (mixtures of toluene/ chloroform and ethanol). In such media, the availability of photogenerated TiO$_2$ conduction-band electrons ($e_{CB}^{TiO_2}$) for reductive pathways is enhanced due to (i) insignificant scavenging of $e_{CB}^{TiO_2}$ and negligible ˙OH radical production due to the absence of dissolved atmospheric O$_2$ and H$_2$O, respectively; and (ii) efficient scavenging of valence-band holes ($h_{VB}^{TiO_2}$) by the solvent (in particular, by ethanol).[32,45] On the basis of a wealth of previous aqueous-phase studies,[23,25,46] the photocatalytic activity of Fe$_x$O$_y$ can be assumed to be irrelevant with respect to that of TiO$_2$. Therefore, mainly the TiO$_2$ component is expected to exploit UV light for chemical reactions.[23,25,46] Our surfactant-capped nanostructured photocatalysts maintained fully soluble and stable, even after prolonged irradiation, due to negligible oxidative degradation of their capping ligands.[47] The high optical transparency of the colloidal systems allowed direct spectrophotometric monitoring of the course of photocatalytic reactions (e.g., related to carrier transfer to target acceptors and/ or catalyst modification) that had a signature in the UV/vis/
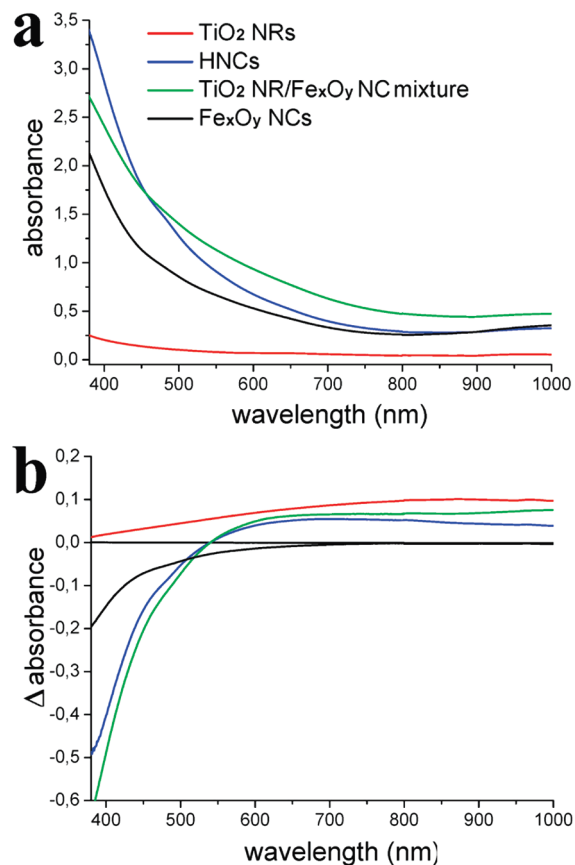
Figure 10. Absorption changes occurring to b-TiO$_2$ NRs (∼5 nm × ∼50 nm), matchstick-like HNCs thereof tipped with ∼10 nm Fe$_x$O$_y$ heads, corresponding NR/Fe$_x$O$_y$ NC physical mixtures, and bare ∼10 nm Fe$_x$O$_y$ NCs, upon UV-irradiation in O$_2$-free conditions: (a) before and (b) after 60 min irradiation. The spectra in panel b were taken using the unirradiated photocatalyst solution as the reference. Conditions: [TiO$_2$] = 0.72 mM, [Fe$_2$O$_3$] = 0.74 mM.

near-IR spectral range, without the complication of separating the catalysts from solution species.[32a,47]

The photochromic response of the samples is illustrated in Figure 10. The initial NR solutions (Figure 10a, red curve) exhibited the typical TiO$_2$ exciton absorption below 380−370 nm,[23] while the TiO$_2$/Fe$_x$O$_y$-containing samples (Figure 10a, green and blue curves) were dominated by the strong Fe$_x$O$_y$ absorption extending from the UV−vis to the near-IR (Figure 10a, black curve), which originates from ligand-to-metal charge-transfer transitions, magnetic-coupled Fe^{3+} ligand field transitions, and pair excitations.[45] The non-negligible absorption in the near-IR region beyond 700 nm, which is absent in γ-Fe$_2$O$_3$, suggested the presence of the less oxidized Fe$_3$O$_4$ phase.[45]

The irradiation experiments realized simultaneous band gap photoexcitation of Fe$_x$O$_y$ and TiO$_2$ components. As a result of efficient $h_{VB}^{TiO_2}$ scavenging by the solvent molecules (Scheme 1, part I), continuous UV-photoexcitation of the b-TiO$_2$ NRs resulted in a net accumulation of $e_{CB}^{TiO_2}$ at Ti(IV) centers.[32,48] This phenomenon was marked by the emergence of a distinguishable featureless absorption in the visible to near-IR range (λ > ∼400 nm, blue coloration), which reached saturation in

(45) (a) Tang, J.; Myers, M.; Bosnick, K. A.; Brus, L. E. *J. Phys. Chem. B* **2003**, *107*, 7501−7506. (b) He, Y. P.; Miao, Y. M.; Li, C. R.; Wang, S. Q.; Cao, L.; Xie, S. S.; Yang, G. Z.; Zou, B. S.; Burda, C. *Phys. Rev. B* **2005**, *71*, 125411.

(46) (a) Sherman, D. M. *Geochim. Cosmochim. Acta* **2005**, *69*, 3249−3255. (b) Pehkonen, S. O.; Siefert, R.; Erel, Y.; Webb, S.; Hoffmann, M. R. *Environ. Sci. Technol.* **2002**, *27*, 2056−2062. (c) Cwiertny, D. M.; Hunter, G. J.; Pettibone, J. M.; Scherer, M. M.; Grassian, V. H. *J. Phys. Chem. C* **2008**, *113*, 2175−2186. (d) Du, W.; Xu, Y.; Wang, Y. *Langmuir* **2007**, *24*, 175−181. (e) Borer, P. M.; Sulzberger, B.; Reichard, P.; Kraemer, S. M. *Mar. Chem.* **2005**, *93*, 179−193.

(47) Cozzoli, P. D.; Comparelli, R.; Fanizza, E.; Curri, M. L.; Agostiano, A.; Laub, D. *J. Am. Chem. Soc.* **2004**, *126*, 3868−3879.

(48) Kamat, P. V. *J. Phys. Chem. C* **2007**, *111*, 2834−2860.

(49) (a) Gotic, M.; Koscec, G.; Music, S. *J. Mol. Struct.* **2009**, *924−926*, 347−354. (b) Sun, Y.-k.; Ma, M.; Zhang, Y.; Gu, N. *Colloids Surf., A* **2004**, *245*, 15−19. (c) Helgason, Ö.; Gunnlaugsson, H.; Steinthorsson, S.; Mørup, S. *Hyperfine Interact.* **1992**, *70*, 981−984.
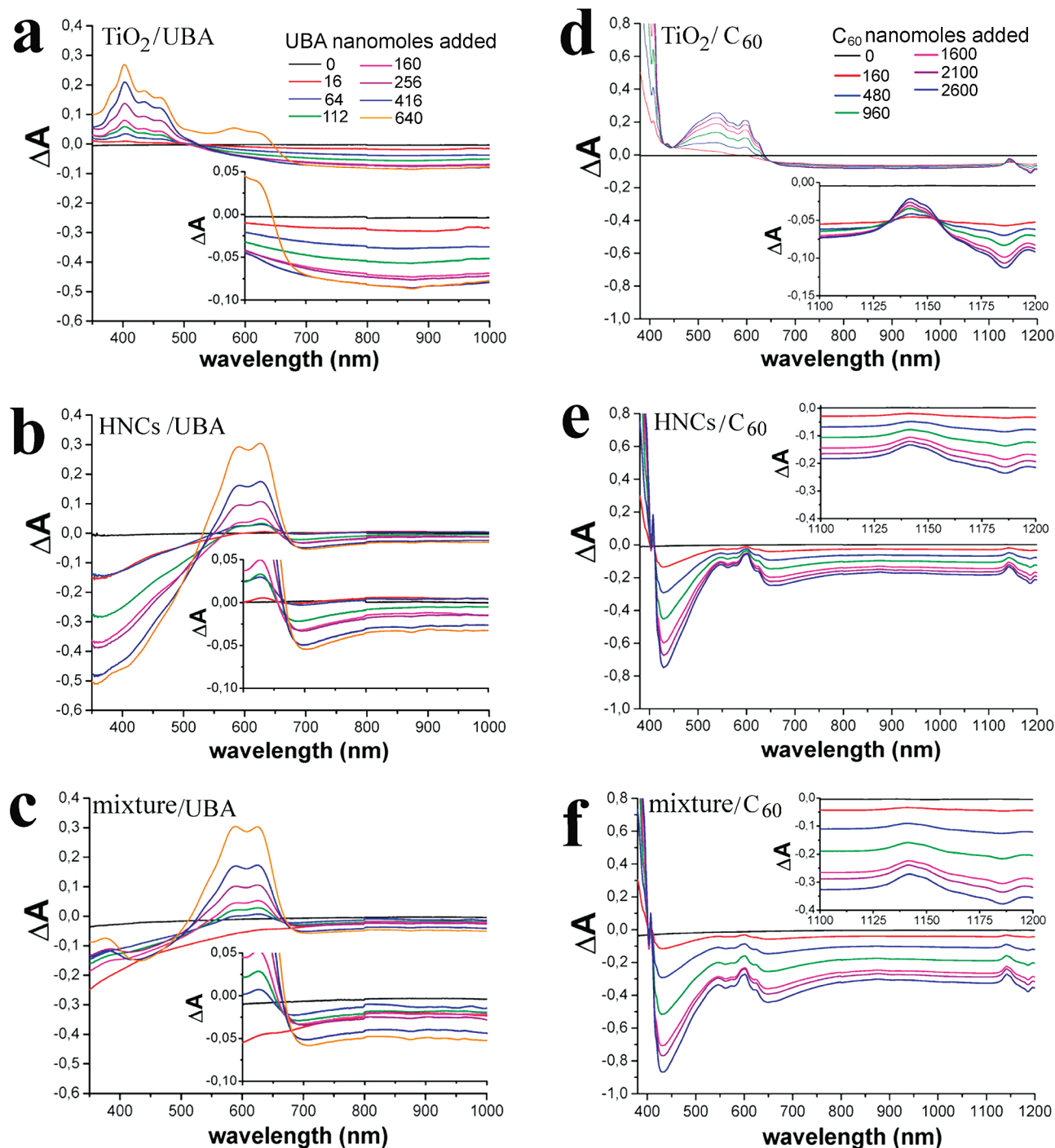
Figure 11. Electron titration experiments: absorption changes occurring to (a,d) preirradiated *b*-TiO₂ NRs (∼5 nm × ∼50 nm), (b,e) matchstick-like HNCs thereof, tipped with ∼10 nm Fe$_x$O$_y$ heads, and (c,f) corresponding NR/Fe$_x$O$_y$ NC physical mixtures upon successive additions of UBA (a−c) or of C₆₀ (d−f) in O₂-free conditions. The spectra were taken using the irradiated photocatalyst solution as the reference (cf., Figure 10b) and were corrected by the relevant dilution factor. Conditions: [TiO₂] = 0.72 mM, [Fe₂O₃] = 0.74 mM; preirradiation time = 60 min (note that the small kinks detectable at 800 nm in some cases are artifacts due to light source switching in the spectrophotometer).

1−3 h, depending on the TiO₂ concentration and on the solvent composition. The difference spectra allow clear visualization of the net changes achieved (Figure 10b, red curve). The $e_{CB}^{TiO_2}$ storage on *b*-TiO₂ NRs was confirmed to be a fully reversible process. Actually, the blue coloration vanished either very slowly (over several hours) if the stored $e_{CB}^{TiO_2}$ were allowed to discharge into the solution under nitrogen or almost instantly if air (hence O₂) was admitted to the vessel.[32]

In the case of the HNCs and TiO₂/Fe$_x$O$_y$ mixtures (Figure 10b, blue and green curves), photochromic changes were also

appreciable, which however took place more slowly (in 3−4 h irradiation) and were distinguished by some major features at saturation. First, the absorbance developing at λ > 500 nm was proportionally less pronounced, according to the order: HNCs < *b*-TiO₂/Fe$_x$O$_y$ mixture < TiO₂, with slope variation being evident at λ > 700 nm. No such absorption was detected for isolated Fe$_x$O$_y$ NCs (Figure 10b, black curve). Second, a significant bleaching emerged at λ < 500, not otherwise detected for *b*-TiO₂, which appeared to be less accentuated for bare Fe$_x$O$_y$ NCs. Complementary investigations, supported by TEM moni-

Scheme 1. Proposed Energy Diagram and Reaction Pathways Involved in UV-Driven Charge Accumulation (I, III) and Subsequent Dark Reduction (II, IV) of Molecular Acceptors (UBA or C_{60}), Which Were Achieved Using Either b-TiO_2 NRs or b-TiO_2–Fe_xO_y HNCs as Photocatalysts in Deaerated Organic Solutions[a]

under UV irradiation

in the dark, after irradiation
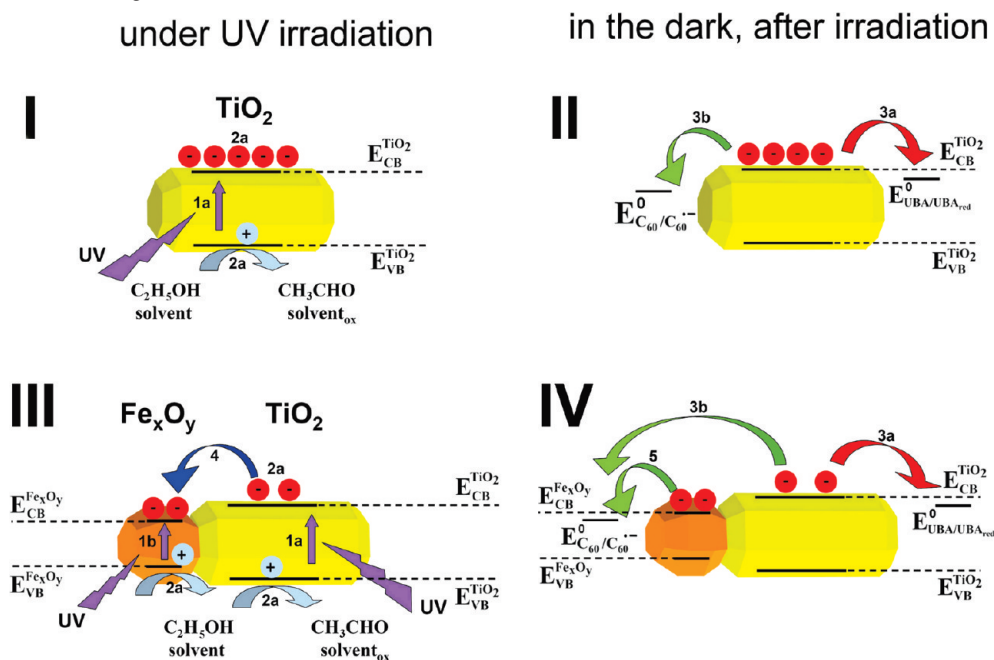
[a] **1**: Band gap photoexcitation and electron−hole pair generation (**1a** ≫ **1b**). **2a**: Hole transfer to the scavenger solvent molecules. **2b**: Electron accumulation in the b-TiO_2 conduction band. **3a**: Electon transfer from reduced b-TiO_2 to UBA. **3b**: Electon transfer from reduced b-TiO_2 to C_{60}. **4**: Electron transfer from photoexcited TiO_2 conduction band to Fe_xO_y. **5**: Electon transfer from reduced Fe_xO_y to C_{60}.

toring of the Fe_xO_y size evolution and ICP-AES analysis of the Fe content in the solution, indicated that Fe_xO_y was not affected by any noticeable photodissolution, a drawback that has instead been frequently encountered for Fe_xO_y photocatalysis in aqueous media, especially in the presence of Fe-ion chelating agents, $h_{VB}^{Fe_xO_y}$ scavengers, and/or in case of direct Fe_xO_y interfacing with TiO_2.[20a,25] The low solubility of Fe^{3+}/Fe^{2+} ions in the relatively nonpolar media used here could be responsible for the observed Fe_xO_y resistance against photocorrosion. Notably, the photoinduced spectral changes relative to the binary photocatalysts were not fully reversible upon air admission to the vessel and displayed further (though much slower) evolution even under inert atmosphere in the dark, suggesting that the preirradiated Fe_xO_y component had become reactive toward the solvent molecule (Figure S11 in the Supporting Information). On the basis of these experimental proofs, the spectral changes at $\lambda >$ 500 nm could be provisionally interpreted (Scheme 1, part III) as arising partly from the effect of excess $e_{CB}^{TiO_2}$ stored on b-TiO_2 and partly from alterations in the electronic structure, stoichiometry, and/or average degree of oxidation of the Fe_xO_y component induced by b-TiO_2 carrier injection (for example, a γ-Fe_2O_3 phase enrichment could lead to absorption changes, especially in the red/near-IR region[45]). Changes in Fe_xO_y electronic structure could be invoked to account for the bleaching at $\lambda >$ 500 nm, the extent of which indeed appeared to be dictated by the interaction of Fe_xO_y with photoexcited TiO_2[45] (cf., black and green/blue curves in Figure 10b).

To clarify the origin of the photoinduced spectral changes, we verified the feasibility of extracting the photoinduced excess of electrons trapped on the preirradiated samples and using them for subsequent reduction reactions in the dark. To probe electron transfer, we used an organic antrachinonic dye, UBA (Figure S1 in the Supporting Information), which can be reduced to its hydroantraquinonic form, UBA_{red} ($+0.1 < E^0_{UBA/UBA_{red}} \approx$

$0.1 \div 0.154$ V vs NHE at pH = 7),[32a,50] and fullerene (C_{60}), the latter being capable of multielectron reduction ($E^0_{C60/C60^{·-}} = -0.25$ V vs NHE for the one-electron C_{60} reduction to $C_{60}^{·-}$),[32b,c,48,51] as efficient electron acceptors that exhibit distinct absorption features in their oxidized and reduced forms, respectively. Assuming that the literature redox potential scale, measured for aqueous media, is valid for our system,[32,47] the energetics is favorable to $e_{CB}^{TiO_2}$ transfer to both acceptors, because the TiO_2 conduction-band edge is more negative ($E_{CB}^{TiO_2} = -0.5$ V vs NHE at pH = 7). On the other side, the position of the conduction-band edge of nanosized spinel cubic Fe_xO_y ($E_{CB}^{Fe_xO_y}$) is uncertain,[20,21,24,25,45a,46,49,52] being expected to be located several tens of meV below $E_{CB}^{TiO_2}$. It can therefore be anticipated that the potential of Fe_xO_y conduction-band electrons ($e_{CB}^{Fe_xO_y}$) eventually available may not be low enough to reduce both acceptors considered here (Scheme 1, parts II, IV).

Electron titration experiments were performed under nitrogen by injecting known acceptor amounts into the UV-irradiated nanostructure solution and recording the differential spectrum after each addition against the UV-irradiated solution as the reference. In the UBA-based titrations, the emergence of new features at ~380, ~400, ~435, and ~465 nm, along with the disappearance of the double band of unreduced UBA (peaking

(50) (a) Cozzoli, P. D.; Fanizza, E.; Comparelli, R.; Curri, M. L.; Agostiano, A.; Laub, D. *J. Phys. Chem. B* **2004**, *108*, 9623–9630. (b) Cozzoli, P. D.; Comparelli, R.; Fanizza, E.; Curri, M. L.; Agostiano, A. *Mater. Sci. Eng., C* **2003**, *23*, 707–713. (c) Vinodgopal, K.; Bedja, I.; Hotchandani, S.; Kamat, P. V. *Langmuir* **2002**, *10*, 1767–1771.
(51) (a) Kamat, P. V. *J. Am. Chem. Soc.* **1991**, *113*, 9705–9707. (b) Kamat, P. V.; Bedja, I.; Hotchandani, S. *J. Phys. Chem.* **1994**, *98*, 9137–9142.
(52) (a) Kontos, A. I.; Likodimos, V.; Stergiopoulos, T.; Tsoukleris, D. S.; Falaras, P.; Rabias, I.; Papavassiliou, G.; Kim, D.; Kunze, J.; Schmuki, P. *Chem. Mater.* **2009**, *21*, 662–672. (b) Laouini, E.; Berghoute, Y.; Douch, J.; Mendonça, M.; Hamdani, M.; Pereira, M. *J. Appl. Electrochem.* **2009**, *39*, 2469–2479.

at 588 and 625 nm), mark the formation of UBA$_{red}$.[32a] In the case of C$_{60}$-based titrations, the generation of C$_{60}^{\cdot-}$ is recognizable by the growth of an extra narrow band with maxima at 1140−1150 nm and absorption bleaching at 1180−1185 nm, which add to the spectral features of unreduced C$_{60}$ (at ∼408, ∼540, and ∼600 nm).[32b,c,51]

The titration results are summarized in Figure 11. In the case of preirradiated TiO$_2$ NR sample, electron uptake by the acceptor was accompanied by a proportional absorption dampening in the visible-to-near-IR region, which confirmed the existence of a photoinduced excess of $e_{CB}^{TiO_2}$ trapped on TiO$_2$ and their prompt utilization in the reduction reaction. In particular, UBA allowed quantitative extraction of the extra $e_{CB}^{TiO_2}$ stored to produce stoichiometric amounts of UBA$_{red}$.[32a] Indeed, the titration end point, marked by the appearance of the double band of unreduced UBA (peaking at 588 and 625 nm), corresponded to full abatement of the visible-to-near-IR absorption that had grown in the UV-irradiation step (cf., Figure 11a). Differently, an incomplete abatement of the visible-to-near-IR absorbance (∼80%) was observed in the C$_{60}$-based titration, as the C$_{60}$/C$_{60}^{\cdot-}$ redox couple attained equilibrium with residual $e_{CB}^{TiO_2}$ resident within TiO$_2$ for relatively large C$_{60}$ amounts added[51] (Figure 11d).

Interesting pieces of information were gathered from the titrations of the Fe$_x$O$_y$-containing samples. The C$_{60}$-based titrations highlighted that the C$_{60}^{\cdot-}$ yield, judged from the net absorbance excursion associated with the local maxima at 1140−1150 nm, was little affected by the presence of the Fe$_x$O$_y$ component (Figure 10e,f). In contrast, the UBA$_{red}$ yields attained using preirradiated physical mixtures and HNCs were found to be, respectively, ∼85% and ∼95% lower than that achieved with TiO$_2$ only (Figure 10b,c). This trend was indirectly confirmed by the relative rate of steady-state photocatalytic UBA demolition reported when coexisting photocatalyst/dye solutions were subjected to continuous UV illumination[50a,b] (Figure S12 in the Supporting Information). By comparison, insignificant acceptor reduction took place with the sole preirradiated Fe$_x$O$_y$ NCs (Figure S13 in the Supporting Information).

In addition to the finding above, some sets of spectral details are worthy to be highlighted. First, the ultimate absorbance abatement recorded in the red to near-IR range (λ > 650 nm) along the titration course far exceeded the extent needed to cancel out the positive absorbance gained in the preirradiation step (cf., Figure 10b and Figure 11b,c, e,f). In the particular case of C$_{60}$, control dark experiments with the sole Fe$_x$O$_y$ NCs showed that these spectral changes were mostly due to C$_{60}$ interacting with Fe$_x$O$_y$ surface (Figure S14 in the Supporting Information). Second, the titration led to an extra deep absorbance bleaching at λ < 500 nm (large enough to overwhelm the spectral signature of reduced acceptor), the features and extent of which depended on the specific photocatalyst concerned. No such extra dampening could be detected for blank experiments in which acceptors were added to either irradiated TiO$_2$ NRs or unirradiated TiO$_2$/Fe$_x$O$_y$ samples (Figure S14 in the Supporting Information).

On the basis of all of the experimental findings above, some major deductions can be drawn. The large discrepancies between the reducing capabilities of the preirradiated HNCs and Fe$_x$O$_y$/TiO$_2$ mixture toward the two selected acceptors, relative to the corresponding performances reported with the bare TiO$_2$ NRs, suggested that the visible-to-near-IR absorbance attained for the binary photocatalysts under UV irradiation did not merely reflect the extent of the photoinduced $e_{CB}^{TiO_2}$ reservoir resident in the

TiO$_2$ component. If this had been the case, proportionally smaller reduction yields should have been recorded when using both C$_{60}$ and UBA probes, because $e_{CB}^{TiO_2}$ had in fact been proven to be capable of reducing both species (Figure 11a,d). Therefore, it should be inferred that, in addition to $e_{CB}^{TiO_2}$ stored within TiO$_2$, some other species acted as selective reducing agents (i.e., capable to drive further reduction of C$_{60}$ only) in the preirradiated composite photocatalysts. The known redox properties of spinel cubic iron oxides suggest that such species could reasonably be the pristine Fe$_x$O$_y$ domains in a reduced Fe$_3$O$_4$-rich form.[21a−e,24,25,32,45a,46,49] Assuming no relevant kinetic barrier for electron release from these UV-reconstructed "magnetite-like" domains, the latter should be assigned a redox potential $E_{CB}^{Fe_xO_y}$ (or, equally, the potential for the γ-Fe$_2$O$_3$/Fe$_3$O$_4$ redox couple, $E_{\gamma\text{-}Fe_2O_3/Fe_3O_4}^0$) lying somewhere below $E_{C_{60}/C_{60}^{\cdot-}}^0$ (Scheme 1, parts II, IV). Finally, the emergence of spectral features that were not correlated with acceptor reduction suggested that the optical properties of UV-activated Fe$_3$O$_4$-like sections could be strongly affected by adsorption of the acceptor molecules and/or their reduced counterparts.

4. Discussion

4.1. Growth Mechanism of HNCs. The present work has demonstrated a colloidal approach for the topologically controlled synthesis of magnetic–semiconductor all-oxide HNCs in an exclusive heterodimer configuration. The newly developed heteronanostructures are individually composed of one rod-like orthorhombic-phase *b*-TiO$_2$ section, on which a single nearly spherical cubic-phase Fe$_x$O$_y$ domain is located either at one apex or at any location along the longitudinal sidewalls. The protocol devised here permits the high-yield preparation of HNCs in specific architectural configurations with the dimensions of constituent material sections being independently tunable over a broad size range by adjustment of a few reaction parameters.

The controllable liquid-phase preparation of surfactant-stabilized heteronanostructures with asymmetric distribution of their constituent domains requires achieving independent control over the fundamental nucleation and growth processes underlying formation of the individual material components, on one side, and operation of suitable anisotropic reaction pathways to allow for topology selection, on the other side.[1] To realize these goals for the present *b*-TiO$_2$/Fe$_x$O$_y$ system, we have implemented a seed-mediated strategy through which Fe$_x$O$_y$ formation by a nonhydrolytic route can be governed by means of preformed *b*-TiO$_2$ NRs in the reaction environment. Within the frame of this scheme, the potential for generating binary *b*-TiO$_2$/Fe$_x$O$_y$ HNCs with simultaneously selectable topologies and geometric parameters arises from the combination of two major conditions: first, the use of specifically shape-tapered *b*-TiO$_2$ NRs equipped with structurally dissimilar apexes, which can potentially act as anisotropically reactive seeding substrates; second, promotion of a kinetically driven Fe$_x$O$_y$ deposition regime, in which the anisotropic reactivity of the seeds can be accentuated so as to guarantee their controllable site-selective accessibility beyond growth limitations imposed by interfacial strain. In the following, these issues will be discussed within the frame of different models offering complementary mechanistic views of HNC formation.

A CNT Interpretation. The time evolution of HNC topology indicates that foreign *b*-TiO$_2$ NRs present in Fe$_x$O$_y$-generating media act as primary nucleation centers onto which Fe$_x$O$_y$ is selectively deposited.[1,19] This mechanism is founded on a basic

principle of the classical nucleation theory (CNT), according to which the energy barrier, ΔG_{het}^*, that has to be surpassed for a given material to nucleate heterogeneously onto a preformed condensed phase (seeds) is lower than the activation energy, ΔG_{hom}^*, required to induce corresponding homogeneous nucleation of separate crystal embryos:[1,34b,37b]

$$\Delta G_{het}^* = f(\theta)\Delta G_{hom}^* \qquad (1)$$

where the "wetting" function, $0 < f(\theta) < 1$, depends on the particular system geometry (e.g., size/shape of the substrate seed and of the material domain "droplet" deposited thereon) and on the interfacial tension equilibrium attained at the three-boundary seed/"droplet"/solution region.[53] In an equivalent way, heterogeneous nucleation can be described as requiring a much lower chemical potential of solution monomers to be triggered, relative to homogeneous nucleation:[34b]

$$\Delta\mu_{het} < \Delta\mu_{hom} \qquad (2)$$

The limiting case of complete "wetting", in which the depositing "droplet" has full affinity to the substrate (i.e., the foreign "droplet" and the substrate are made of the same material), corresponds to the process of seed growth.[53] The latter involves a proportionally negligible barrier, ΔG_{growth}^* ($\Delta G_{growth}^* \ll \Delta G_{het}^* < \Delta G_{hom}^*$), and can accordingly be sustained by much lower supersaturation levels ($\Delta\mu_{growth} \ll \Delta\mu_{het} < \Delta\mu_{hom}$).

The synthesis of the present TiO_2–Fe_xO_y HNCs has been based on coupling a seeding step with a particular Fe_xO_y-generating route that meets nucleation–growth kinetic requirements suitable to realize the potential of the seeded growth approach.[33] We have exploited the thermal treatment of $Fe(CO)_5$ in a complex OLAM/OLAC/DDIOL mixture, whereby various nonhydrolytic pathways, such as direct pyrolysis of in situ formed iron oleate and/or amino iron complexes and aminolysis/alcoholysis of iron oleate, can yield different Fe and Fe_xO_y phases, depending on the reaction conditions.[33] Our experiments were performed at moderate temperature without addition of extra oxidizers, which guaranteed selective production of inverse spinel Fe_3O_4/γ-Fe_2O_3, as proven by combined SR-XRD, HRTEM, and XANES investigations (Figures 2, 6–8). Fe_xO_y formation in these nonaqueous surfactant systems involves a distinctive reaction dynamics arising from the dissimilar dependence of the nucleation and growth processes on temperature and on the solution supersaturation degree, respectively.[33a,b,d] In the absence of foreign seeds, homogeneous nucleation is a highly hindered process that can be considerably delayed with respect to the nominal precursor injection step until a sufficiently high concentration of secondary molecular species has ac-

cumulated in the solution.[33a,d] It manifests as a sudden burst-like event that self-terminates as the monomer supersaturation is quickly relieved below the critical level required to surpass the huge $\Delta G_{hom}^{Fe_xO_y}$ barrier. On the other hand, once embryos have been formed, their further growth proceeds autocatalytically ($\Delta G_{growth}^{*Fe_xO_y} \ll \Delta G_{hom}^{*Fe_xO_y}$) in a diffusion-controlled regime leading to fast volume increase and size focusing.[33b,d]

The formation of HNCs can be rationalized within the frame of the above-described nucleation–growth dynamics as it is "perturbed" by the presence of preformed seeds.[1,19] Selective Fe_xO_y deposition onto foreign b-TiO_2 NRs is ensured by an initial fast iron precursor injection that induces a slow increase in the monomer chemical potential up to the modest level $\Delta\mu_{het}^{Fe_xO_y}$ required for narrowly overcoming the low $\Delta G_{het}^{*Fe_xO_y}$ barrier. During this stage, the Fe_xO_y monomers are swiftly consumed, and further depletion occurs during subsequent autocatalytic Fe_xO_y growth.[33] Parasitic homogeneous nucleation is eluded because it needs a much higher solution supersaturation level to earn the energy surplus necessary to surpass $\Delta G_{hom}^{*Fe_xO_y}$ (eq 2).

A relatively broad size variance generally characterizes the Fe_xO_y domains of the as-borne HNCs at the early development stages, depending on the absolute precursor to seed ratio realized in the primary injection (cf., Figure 5). This fact suggests that both the apex-confined surface regions and longitudinal side-walls of the NRs should accommodate a distribution of differently reactive sites,[11,14,17,54] actually reflecting the rich seed faceting evidenced by HRTEM (Figures 1 and 3). Irregularities in surface atomic arrangement, defects, corners, edges, and/or regions of imperfect surfactant passivation are likely to act as primary catalytic centers capable of triggering the deposition process. The drop in supersaturation level caused by fast monomer consumption during the early reaction stages can explain why heterogeneous nucleation could not be reiterated after the primary event. In addition, it is conceivable that the concomitant buildup of an electric polarization region at the newly formed b-TiO_2/Fe_xO_y interface could adversely alter the charge distribution across the seed so as to drive exclusive growth of the primarily implanted Fe_xO_y domain rather than initiating deposition at additional seed locations.[6,17c,19] Both effects can explain why HNCs are ultimately composed of a single Fe_xO_y domain accommodated on each b-TiO_2 NR over a wide range of synthesis conditions. This picture justifies the technique of replenishing the Fe_xO_y monomer availability by means of slow supplementary reactant additions, which conveniently served to propel selective enlargement of the Fe_xO_y sections to extremely large sizes (~40 nm), while permitting narrowing of their size distribution.

Overall, the above-described dynamics, whereby the b-TiO_2 seeds regulate the relative extent of Fe_xO_y monomer consumption between a kinetically hindered heterogeneous nucleation phase and a self-catalyzed growth stage, accounts for the high yield with which binary HNCs can be obtained in exclusive heterodimer configuration with independently size-tunable component material sections.

A Thermodynamic Description. In a more accurate thermodynamic description, the Fe_xO_y "wetting" condition on b-TiO_2 can be expressed by evaluating the sign of total free surface energy change, ΔG_S, that accompanies heterogeneous deposition, in close analogy with the description of thin-film hetero-

(53) The universal relation holding between ΔG_{het}^* and ΔG_{hom}^* (eq 1) has been clarified within the frame of simplified models (see refs 34b, 37b), in which a "nucleus" of a secondary material (Fe_xO_y in the present case) heterogeneously deposited on a pre-existent seed (b-TiO_2 in our case) is regarded as a "droplet" that has condensed thereon, forming a contact angle, θ, with the substrate underneath: $\Delta G_{het}^* = f(\theta)\Delta G_{hom}^*$, where the wetting function, $f(\theta)$, that defines the degree of "wetting" achievable is $0 < f(\theta) < 1$, and depends on the particular system geometry (e.g., shape of the substrate and of the droplet) and on the interfacial tension equilibrium attained at the three-boundary TiO_2/Fe_xO_y/solution region according to the Young's relation: $\sigma_{TiO_2} = \sigma_{Fe_xO_y}\cos\theta + \sigma_{TiO_2/Fe_xO_y}$, where σ_{TiO_2} and $\sigma_{Fe_xO_y}$ are the specific solid/solution tensions associated with the two materials, and σ_{TiO_2/Fe_xO_y} is the specific solid/solid TiO_2/Fe_xO_y tension. Note that the barrier for nuclei growth, ΔG_{growth}^*, is far smaller than both ΔG_{hom}^* and ΔG_{het}^* and corresponds to the limiting case of complete wetting ($f(\theta) \rightarrow 0$ for $\theta \rightarrow 0$).

(54) Casavola, M.; Falqui, A.; Garcia, M. A.; Garcia-Hernandez, M.; Giannini, C.; Cingolani, R.; Cozzoli, P. D. *Nano Lett.* **2009**, *9*, 366–376.

structure growth onto crystallographically oriented substrates performed by classical vapor-phase techniques:[40]

$$\Delta G_S = \gamma_{TiO_2} - \gamma_{Fe_xO_y} + \gamma_{TiO_2/Fe_xO_y} \qquad (3)$$

where γ_{TiO_2} and $\gamma_{Fe_xO_y}$ are the solid/solution interfacial energies associated with the respective materials (also referred to as surface energies in the case of colloidal NCs), and γ_{TiO_2/Fe_xO_y} is the solid/solid interfacial energy. The former two terms can be expected to be affected by adhesion of solution species, while the latter depends on the bonding strength and lattice mismatch.[40]

The structural-topological complexity of the present heterostructures does not allow identification of a unique "wetting" regime, because the starting substrate seeds expose various sets of facets with different extension, which can covered by Fe_xO_y either completely ($\Delta G_S > 0$), that is, at the NR apexes, or partially ($\Delta G_S < 0$), that is, at the longitudinal sidewalls. The nonnegligible interfacial strain should play important roles in driving Fe_xO_y to segregate into discrete spherical domains rather than ubiquitously covering the whole seed surface.[1,3−19]

The success of our seeded syntheses indicates that the formation of HNCs is energetically favorable under our reaction conditions, because it permits the total free surface energy to be lowered below the value that would otherwise characterize a solution mixture of NRs and homogeneously nucleated tiny Fe_xO_y clusters. The expected energy gain can be understood as arising from a compensation mechanism by which the surface and interfacial energy terms balance with each other. On a first approximation, it can be assumed that the surface energy cost associated with Fe_xO_y deposition, $\gamma_{Fe_xO_y}$, is little dependent on the HNC topology provided that the Fe_xO_y and b-TiO₂ sections share comparable interfacial areas. Therefore, Fe_xO_y nucleation at the NR tips can be regarded as a process that conveniently eliminates the smallest unstable b-TiO₂ facets thereon (cf., Figures 3 and 6). This would lead to a significant γ_{TiO_2} decrease that can largely offset the $\gamma_{Fe_xO_y}$ and γ_{TiO_2/Fe_xO_y} costs due to the creation of the new Fe_xO_y surface and of a highly strained TiO₂/Fe_xO_y junction, respectively. The dissimilar faceting structure at the opposite basal sides of the NRs would explain why Fe_xO_y is ultimately localized on a single apex, likely corresponding to the one at which the excess free surface energy can be minimized. On the other side, for Fe_xO_y to be deposited onto the longitudinal sidewalls of NRs, where more stable low-energy b-TiO₂ facets are present and less strained TiO₂/Fe_xO_y heterojunctions may be attained (cf., Figures 3 and 7), a proportionally smaller γ_{TiO_2/Fe_xO_y} cost has to be paid, which could be satisfactorily compensated for even by the moderate γ_{TiO_2} reduction. Taken together, these arguments suggest that the different HNC topologies can be all expected to be equally probable in terms of interfacial strain energy being counterbalanced by a proportionally adequate reduction in surface energy.

Role of Interface Structure and Misfit Strain. Brookite (orthorhombic) TiO₂ and inverse spinel (cubic) Fe_xO_y are featured by remarkably different crystal structure and lattice parameters, resulting in relatively high interfacial lattice mismatch between the joint material domains regardless of the specific topological arrangement. Fe_xO_y deposition can be therefore expected to be accompanied by the progressive build-up of increasingly large misfit strain energy, the ultimate effect of which being to limit the extension of the b-TiO₂/Fe_xO_y bonding junction as well as to inhibit Fe_xO_y growth to fairly larger sizes.[1,19] As was actually proven by our detailed HRTEM-GPA analyses (Figures 6 and 7), HNCs formation is achieved at the cost of significant extra distortion being induced in the NR section that attains coherent connection to a Fe_xO_y domain. However, the possibility to synthesize HNCs equipped with Fe_xO_y domains as large as ∼40 nm (Figures 4 and 5) without interface dislocations suggests that here misfit strain may impose less stringent constrains on HNC formation than those concerned with their heterostructure counterparts grown from TiO₂ seeds with different structural features.[19] For example, in the case of Fe_xO_y nucleated on anatase TiO₂ NRs, an interfacial mismatch as high as 13% could, in fact, be tolerated to the detriment of significant bending being conferred to the NR section and of Fe_xO_y domain size restriction down to ∼15 nm.[19a] On the other hand, starting from rectangular-shaped b-TiO₂ NR seeds, unstrained b-TiO₂/Fe_xO_y HNCs equipped with Fe_xO_y domains as large as ∼30 nm could be fabricated, the number and the location of which remaining uncontrollable.[19b]

The characteristics of the interfacial region between Fe_xO_y and b-TiO₂ should therefore play an important role in Fe_xO_y deposition mode, while also offering some pathways for misfit strain alleviation. Certainly, as perfect epitaxial growth of a cubic-phase Fe_xO_y on top of an orthorhombic TiO₂ substrate is unlikely to occur, the relevant interface may be expected to be highly defective on the atomic scale. As suggested for other HNC systems,[11a−c,12] the actual junction at each TiO₂/Fe_xO_y heterojunction could be thought of as being built up by a three-dimensional combination of several pairs of facets of the respective materials rather than developing sharply along a single couple of planes that would extend along the entire junction. Such an intricate interface arrangement seems to be plausible in light of the rich faceting and surface irregularity of the NRs, especially at their apexes, and of the significant dissimilarity between TiO₂ and Fe_xO_y lattices. A complex heterojunction structure, whereby the interlocking of multiple facet couples results in a boundary region with nanometer-scale roughness, could provide convenient pathways for relieving strain that may be generated locally along specific plane associations. Strain relaxation could be achieved, for instance, by local near-interface plane bending or via elastic redistribution across less detrimentally mismatched neighboring junctions and consequent propagation far from the interfacial region. Actually, our HRTEM experimental insight complemented by interface modeling (Figures 6 and 7) has suggested that the coherent attachment between the b-TiO₂ and Fe_xO_y domains realizes strain compensation through three-dimensional association of heterointerfaces, each characterized by different lattice matching degree.[11a−c,12,15] In support of this picture, our HRTEM-GPA strain maps have pointed out that the lattice-mismatched conditions attained at b-TiO₂/Fe_xO_y bonding junctions cause the b-TiO₂ section of the HNCs to experience noticeable extra tension that concentrates at the interface edges and propagates far away from the near-junction region deeper into the seed portion adjacent to the Fe_xO_y. It is remarkable that the strain signature ultimately spans a b-TiO₂ seed area twice as extended as that shadowed by Fe_xO_y domains, beyond which it vanishes more or less abruptly, leaving the remaining b-TiO₂ section virtually undistorted. The lattice compression or dilatation experienced by the decorated b-TiO₂ NRs is an effect clearly distinct from the deformation associated with its pre-existent longitudinal curvature, which concertedly varies to only a negligible extent (cf., Figure 3). In this regard, it is conceivable that, in addition to the attainment of a nanoscale-roughened junction region, other circumstances favorable to efficient withstanding of strain could be provided

by the inherent geometric features of the seeds. Curved b-TiO$_2$ NRs with small diameter and high aspect ratios, like those exploited here, could, on one side, offer better local lattice matching conditions for Fe$_x$O$_y$ deposition and, on the other side, act as elastically deformable platforms across which interfacial strain can be dissipated remotely, circumventing plastic relaxation via defect generation.[40] Lattice expansion or contraction in the curved NRs represents the sole price that the heterostructured system has to pay to achieve coherent b-TiO$_2$/Fe$_x$O$_y$ attachment without formation of misfit dislocations at a proportionally much smaller cost of increased surface energy.[1,19a,15,40,54] On the other end, on the basis of previous investigations,[19a] significant accentuation of the pristine curvature of the seeds should have been expected to take place only in response to much higher misfit values than those assessed for the present heterostructures.

The formation of HNCs in an exclusive heterodimer configuration can also be rationalized on the basis of the strain energy argument above. Indeed, intensification and far-from-interface propagation of strain fields along the rapid growth of the primarily nucleated Fe$_x$O$_y$ domain can be expected to render the seed underneath less prone to tolerate additional mismatched heterojunctions. This could accordingly explain why reiteration of Fe$_x$O$_y$ deposition events on individual NRs was never achieved even when heterostructure growth was propelled by excess reactant feeding. A similar impact on HNC growth mode was reported for Fe$_x$O$_y$ grown with straight, low aspect-ratio anatase TiO$_2$ NRs, which acquired curvature in response to extreme misfit strain, ultimately permitting accommodation of only a single Fe$_x$O$_y$ domain per seed.[19a] Another factor preventing multiple heterogeneous nucleation could be the strain-driven modification of the inner permanent electric dipole associated with one-dimensional nanostructures with noncentrosymmetric or deformed lattice,[14,17c,55] which would result in an inhibitory influence similar to that caused by b-TiO$_2$/Fe$_x$O$_y$ interfacial polarization effects invoked previously.

Mechanism of Heterostructure Topology Selection: A Kinetic Argument. The most remarkable achievement demonstrated by the present synthetic approach is represented by the possibility of switching the HNCs topology from a specific matchstick-like to a nonselective configuration, where the TiO$_2$ and Fe$_x$O$_y$ domains are randomly arranged.

In earlier reports on the synthesis of single-tipped matchstick- or double-tipped dumbbell-like HNCs, the strong preference for a foreign material to nucleate onto the apexes of NR seeds was assumed to be intrinsically consistent with the mechanism of their anisotropic growth. According to the latter, the NR tips should correspond to the fastest-growing lattice directions, as they accommodate facets with much higher chemical reactivity and/or ineffective surfactant passivation.[1,10−18] However, a few approaches have so far allowed a given NR seed to be decorated with a different material domain at selected locations in a controllable manner. This opportunity has been shown to be viable for systems in which seed accessibility is strictly controlled by the ligand concentration[15,17a] or unusual intraparticle ripening mechanisms are operative.[11]

The results reported for the present b-TiO$_2$/Fe$_x$O$_y$ heterostructures illustrate a clear case where topological control can be achieved by associating seeds with suitable structural requirements with a particular reaction kinetics regime. This is highlighted by the following observations.

First, the injection-modulated experiments (Figure 5) have pointed out that the Fe(CO)$_5$ to b-TiO$_2$ seed molar ratio realized in the primary fast precursor addition step regulates the site selectivity achievable, that is, the yield of matchstick HNCs relative to other heterostructure types, as well as the size of the Fe$_x$O$_y$ domains initially formed at the respective locations. These findings imply that the probability of heterogeneous Fe$_x$O$_y$ nucleation and the rate at which the latter takes place depend on the particular b-TiO$_2$ seed sites available, to an extent that is dictated by the initial degree of solution supersaturation. In particular, the NR tips appear to be the most reactive locations at high nominal Fe(CO)$_5$ to b-TiO$_2$ molar ratios, while the longitudinal sidewalls become progressively more accessible at lower precursor concentration (cf., Figures 4 and 5). Thus, although the tapered b-TiO$_2$ NRs may possess spatially anisotropic accessibility toward Fe$_x$O$_y$, nevertheless such potential reactivity does require high monomer fluxes to be boosted.

Second, it should be considered that the possibility of governing the HNC topology remained prohibited for syntheses seeded with other types of shape- and crystal-phase-tailored TiO$_2$ NCs in similar surfactant environments. For example, the use of anatase NRs (short/long axis: 3−4 nm/20−30 nm), which possessed stepped longitudinal sidewalls and flat basal sides,[56] led to topologically uncontrolled heterodimer HNCs,[19a] while rectangular-shaped b-TiO$_2$ NRs (short/long axis tunable between 3−10 and 30−200 nm, respectively), which were enclosed by smooth longitudinal surfaces and rounded or flat apexes,[27] afforded hetero-oligomer HNCs made by multiply Fe$_x$O$_y$-functionalized NRs with randomly positioned Fe$_x$O$_y$ domains.[19a] On comparing the reactivity of the present shape-tapered b-TiO$_2$ NRs with that of their rectangular-shaped counterparts,[19a] it emerges that even anisotropically shaped seeds with nominally identical sizes, crystallographic structure, and lattice orientation can exhibit remarkably different seeding capabilities, depending on subtle differences in their respective morphological profiles. In this respect, it appears clear that the availability of unique sets of small facets at the arrow-like terminations of the tapered b-TiO$_2$ NRs should be at the basis of their superior versatility as seeds for spatially selective Fe$_x$O$_y$ deposition.

As a matter of fact, neither the CNT arguments (eqs 1 and 2) nor the surface energy balance criterion of heteroepitaxial growth (eq 3) can satisfactorily explain which spatial architecture the HNCs will be ultimately adopt for a given set of experimental conditions. Actually, as discussed earlier, the b-TiO$_2$/Fe$_x$O$_y$ junction arrangements, which we have most frequently observed, appear to be all equally convenient in terms of the surface-interface energy change associated with their formation, as well as in terms of efficiency of interfacial strain energy dissipation. Therefore, rationalization of the observed dependence of HNC topology on the initial b-TiO$_2$ NR to Fe(CO)$_5$ ratio would imply that the "wetting" condition described by eqs 1,2 or eq 3 should be fulfilled selectively for either a matchstick-like or the random heterodimer HNC configuration in response to alterations in the reaction environment.

It could be presumed that a variation in the initial b-TiO$_2$ to Fe(CO)$_5$ ratio could be accompanied by changes in the relative proportions of the NRs to free surfactants and Fe-surfactant complexes in the growing environment. Facet-preferential adhesion of such species to the seeds as well as to the growing

(55) (a) Li, L. S.; Alivisatos, A. P. *Phys. Rev. Lett.* **2003**, *90*, 097402. (b) Morello, G.; Della Sala, F.; Carbone, L.; Manna, L.; Maruccio, G.; Cingolani, R.; De Giorgi, M. *Phys. Rev. B* **2008**, *78*, 195313.

(56) (a) Cozzoli, P. D.; Kornowski, A.; Weller, H. *J. Am. Chem. Soc.* **2003**, *125*, 14539–14548. (b) Caputo, G.; Nobile, C.; Kipp, T.; Blasi, L.; Grillo, V.; Carlino, E.; Manna, L.; Cingolani, R.; Cozzoli, P. D. *J. Phys. Chem. C* **2008**, *112*, 701–714.

Fe$_x$O$_y$ domains could affect $f(\theta)$ in eq 1 or, equally, the γ_{TiO_2} and $\gamma_{\text{Fe}_x\text{O}_y}$ terms in eq 3, in turn influencing the ultimate surface-interface energy balance that may dictate the preference for either HNC topologies. However, such hypothesis is discredited by our systematic scrutiny of the effect of various reaction parameters on the product outcome, which confirmed that the correlation between the HNC topology and the initial b-TiO$_2$ to Fe(CO)$_5$ ratio was maintained irrespective of the reactant composition over the wide range (even under circumstances leading to undesired homogeneous nucleation of separate Fe$_x$O$_y$ NCs). In this regard, it is plausible that the particular ternary ligand environment used for stabilizing the HNCs builds up a robust organic shell around the NRs, which cancels out any expected spatially differential accessibility already at low stabilizer concentration.

It is also notable that the HNCs do not undergo any topological transition after the initially nucleated Fe$_x$O$_y$ domains have completed their growth and/or the monomer concentration has been replenished by supplemental reactant additions, in contrast to what has been reported for heterostructures based on noble metals and metal chalcogenide materials.[5,11,18] Actually, taking into account the nonhydrolytic condensation pathways leading to Fe$_x$O$_y$ formation and the chemical stability of both TiO$_2$ and Fe$_x$O$_y$ under our reaction conditions, redox or atomic exchange reactions are unlikely to come into play and drive interconversion between different topologies.

The microscopic origin of the growth modes of the present TiO$_2$/Fe$_x$O$_y$ HNCs can be clarified by complementing the thermodynamic picture with kinetic arguments. We propose that the current results can be better rationalized within the frame of a diffusion-controlled growth model, analogous to the one used to account for the anisotropic shape evolution of metal chalcogenide NCs as a function of the relevant monomer concentration in the growing medium.[34,36]

Actually, the hypothesis of HNC growth being governed by reaction-controlled mechanism is in apparent contrast with our experimental evidence. In fact, if Fe$_x$O$_y$ heterogeneous nucleation were the rate-limiting step, the Fe$_x$O$_y$ monomer concentration should be constant throughout the bulk solution as well as in proximity of the NRs. Assuming that Fe$_x$O$_y$ monomers generated through the primary injection step suffice to raise the solution chemical potential beyond the level corresponding to the seed lattice atoms, then the Fe$_x$O$_y$ deposition rate at each NR facet should be proportional to its reactivity and surface area, as well as to the monomer concentration. Apparently, this picture cannot explain the exclusive formation of binary HNCs in heterodimer-like configuration, whereas it would instead predict similar distribution of heterostructure topologies for samples grown under varying precursor supply. In addition, within the frame of a reaction-limited model, syntheses that are performed combining large, high aspect-ratio seeds with high Fe(CO)$_5$ loading should yield multiply decorated hetero-oligomer HNCs, in which the tip-localized Fe$_x$O$_y$ domains differ in size from those grown at the sidewalls of their NR section. However, such heterostructure types were never observed by us (Figures 4 and 5).

We suggest that a diffusion-controlled growth mechanism[1,34,36] can provide a better basis for rationalizing HNC formation and their switchable topology, as sketched in Scheme 2.

Let us first consider the situation of the seeded solution environment prior to Fe(CO)$_5$ injection. In the hot surfactant mixture without any molecular source of crystal-building monomers, the NRs can be expected to become susceptible to

Scheme 2. Sketch of the Proposed Diffusion-Controlled Mechanism of HNC Topology Selection as a Function of the b-TiO$_2$ NR Seed to Fe$_x$O$_y$ Precursor Ratio^a
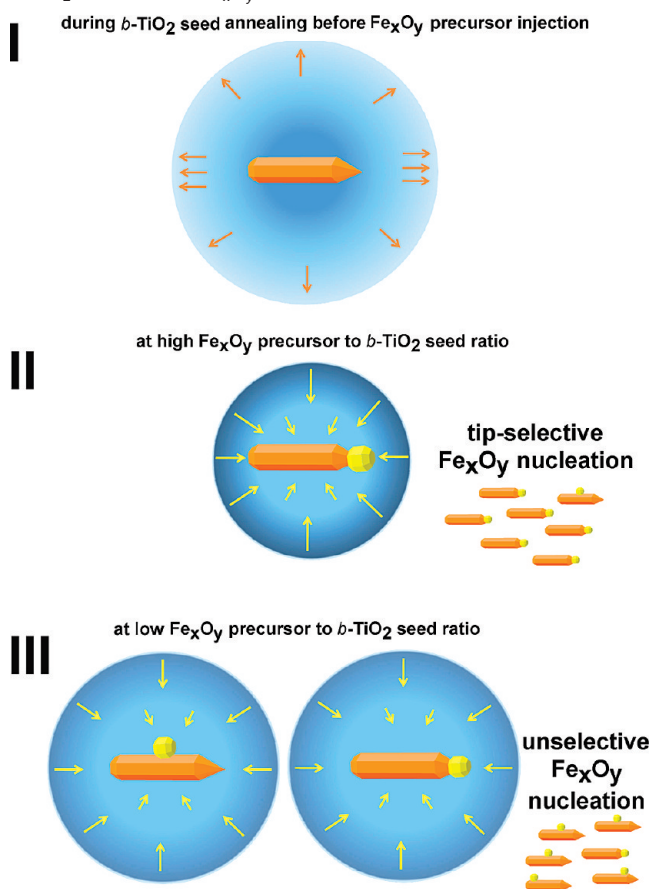
^{a} The circle in each stage represents the interface boundary between the bulk solution and the diffusion sphere. The color shade of the circle indicates the monomer concentration gradient within the diffusion sphere. Orange and yellow arrows denote the diffusion direction and relative intensity of the b-TiO$_2$ and Fe$_x$O$_y$ monomer fluxes, respectively.

slight etching as a means of re-equilibrating the chemical potential of the relevant constituent species (i.e., the b-TiO$_2$ monomers in this case) in the crystalline solid and solution phases, respectively. This phenomenon would result in a stagnant liquid layer around the NRs, across which a b-TiO$_2$ monomer flux directed from the seed outward should lead to a concentration gradient, with the monomer concentration approaching zero at the interface between the diffusion region and bulk solution (Scheme 2, part I). The high cohesive energy of the TiO$_2$ lattice, the stabilizing action of the surface-bound surfactants, the low diffusion coefficient of monomer species coordinated by long-chain organic stabilizers, and the short annealing time that precedes Fe(CO)$_5$ injection would concur to generate an overall rather smooth gradient, whereby an extremely low b-TiO$_2$ monomer concentration suffices to maintain the solubility equilibrium for the NRs without compromising their size and structure appreciably. Under these circumstances, the diffusion sphere front would tend to advance rather slowly over time, and the small seed concentration would minimize the probability of overlapping of neighboring diffusion spheres. In any case, the system would be largely preserved from entering any interparticle Ostwald ripening regime, because TEM monitoring indicated retention of the NR shape and dimensions.

One important aspect of the above picture concerns the spatial inhomogeneity of the diffusion gradient around the NRs.[34b,36b] Indeed, because of their small extension, imperfect ligand passivation, and inherently higher surface energy, the unique facets at the arrow-shaped terminations of the NRs should be inherently characterized by a comparatively higher chemical potential than that of other facets.[36] Consequently, a steeper b-TiO$_2$ monomer concentration gradient and a faster diffusion flux would be established across the solution layer in proximity of the NR apexes, relative to other seed regions. These conditions will have significant implications in the mechanism of HNC formation initiated by subsequent rapid injection of Fe$_x$O$_y$ precursors. It can actually be considered that, upon slow reaction of Fe-surfactant complexes, the bulk solution should become progressively enriched with Fe$_x$O$_y$ monomers, which would raise the average chemical potential well beyond that in the stagnant solution at any facet of the NRs (Scheme 2, parts II−III). The Fe$_x$O$_y$ monomers should tend to transfer across the interfaces of the diffusion spheres toward the NRs inside. The pristine mild seed-to-solution flux of the NR-detaching b-TiO$_2$ monomers would be readily counterbalanced and soon reversed back into an extremely more intense flux of dominant Fe$_x$O$_y$ monomers rapidly diffusing in the opposite solution-to-seed direction.[34,36] These events would cause a significant volume contraction of the diffusion layer and establish internal gradients along which the Fe$_x$O$_y$ monomer concentration will abruptly decrease on approaching the seed surface (Scheme 2, parts II and III).

It is worth stressing that the steepness of the Fe$_x$O$_y$ monomer gradient as well as the monomer migration rate across the diffusion layer will be proportional to the Fe(CO)$_5$ amount introduced in the bulk liquid through the primary fast-injection step. This condition provides a rationale for explaining the origin of topology controlled growth of HNCs. In line with the Mullins−Sekerka kinetic instability model,[34b,37] it can be assumed that the facets, edges, and corners at the unique arrow-shaped apexes of tapered NRs will protrude into zones of the diffusion sphere where they can experience a higher concentration and faster diffusion of Fe$_x$O$_y$ monomers than the rest of the seed surface. At a high Fe(CO)$_5$ to NR molar ratios, the spatial extension of the diffusion layer would be sufficiently reduced, and the gradient across it would be consequently accentuated, so that $\Delta G_{\text{het}}^{*\text{Fe}_x\text{O}_y}$ for heterogeneous Fe$_x$O$_y$ nucleation at the NR tips could be lowered due to the higher degree of local supersaturation and swift monomer supply available thereon than at other seed locations (Scheme 2, part II). As a consequence, Fe$_x$O$_y$ deposition can be preferred at the NR apexes, whereby the structural dissimilarities of the two opposed terminations will pose the basis for a one-sided Fe$_x$O$_y$ decoration mode. In an analogous description, the matchstick-shaped HNCs can be regarded as a kinetically favored heterostructure product resulting from fast Fe$_x$O$_y$ nucleation overdriven by high monomer fluxes.[36] Actually, the tip-selective Fe$_x$O$_y$ deposition can be thought of as sharing the same formation dynamics as that propelling the one-dimensional-only expansion of anisotropic NCs along their fastest-growing lattice directions under an extremely high chemical potential environment.[36] In this picture, the particular structural profile of the seeds at their terminations represents an essential prerequisite to fully profit from diffusion-driven mechanism as a route toward topological selectivity. This is clearly highlighted by the impossibility to observe tip-specific Fe$_x$O$_y$ nucleation either on tapered b-TiO$_2$ NRs that exceed a certain dimensional threshold (Figure 4) or

on their rectangular-shaped counterparts that are enclosed with equally perfected facets both at the tips and at their longitudinal sidewalls.[19b,27]

On the other hand, when the primary fast-injection step sets progressively lower Fe(CO)$_5$ to seed molar ratios in the reaction environment (Figure 5), milder Fe$_x$O$_y$ monomer diffusive fluxes should be generated, and the diffusion layers should become comparatively more extended in space, with the associated concentration gradient turning smoother.[36] Because of the less pronounced spatial inhomogeneity of the chemical potential within the diffusion region, differences in surface accessibility among the exposed seed facets will tend to be gradually canceled out, thereby enhancing the probability of Fe$_x$O$_y$ nucleation at sites other than the NR tips (Scheme 2, part III). The decreasing fraction of matchstick-like HNCs in favor of longitudinally decorated HNCs, along with the vanishing of the site-dependence of the Fe$_x$O$_y$ domain size in response to progressive reduction in precursor supply, well reflects the tendency of the system to approach a Fe$_x$O$_y$ deposition regime that is more under thermodynamic control.[34b,36] In such regime, the HNC population should be characterized by a distribution of topologies matching with the relative energy stability order for the concerned HNC arrangements. Accordingly, as the different HNC configurations have been rationalized to have a similar probability of formation on the basis of surface-interface energy arguments, no selectivity for Fe$_x$O$_y$ localization on the b-TiO$_2$ seeds should be observable, as experimentally proven. In an equivalent mechanistic picture, the transition from the tip-selective to nonspecific Fe$_x$O$_y$ deposition mode can be considered as sharing the same origin as that suggested for the shape evolution of anisotropic semiconductor NCs, whereby the initial kinetically overdriven one-dimensional-only development switches to a thermodynamically governed equidirectional growth regime upon progressive exhaustion of the feeding monomers.[34b,36]

After the heterogeneous nucleation burst, self-catalyzed reaction and consumption of reactive monomers in proximity of the primary Fe$_x$O$_y$ patches will cause their further depletion thereon and sustain development of the Fe$_x$O$_y$ domains. Over time, the diffusion layer should extend in space, and the overall growth rate will slow as the concentration gradient becomes smoother. However, the Fe$_x$O$_y$ domains would always protrude further in regions of the diffusion layer characterized by comparatively higher supersaturation, keeping on growing the fastest due to the negligible $\Delta G_{\text{growth}}^{*\text{Fe}_x\text{O}_y}$ barrier. This can make Fe$_x$O$_y$ growth process self-sustain, ultimately circumventing extra deposition events.

4.2. Magnetic Properties. Another interesting result of this study is that the HNCs no longer exhibit the characteristic magnetic behavior of otherwise isolated spinel Fe$_x$O$_y$ NCs, which would be dictated solely by finite size and surface effects in the dimensional regime addressed here.[33b−d,42b,44] We found that, although neither H_C, M_S, nor T_B could individually be traced to any clear size-dependent trend, however, they all followed a very similar dependence on the dimensions of the Fe$_x$O$_y$ component (Figure 9). These results suggest that the properties of the HNCs should ultimately be governed by the "effective magnetic volume" of the Fe$_x$O$_y$ domains, being dictated by their nominal size, the surface-to-volume ratio, and the extension of the actual TiO$_2$−Fe$_x$O$_y$ domains bonding region. This interpretation is consistent with the observation that the magnetic behavior of the HNCs deviated from that of corresponding NR/Fe$_x$O$_y$ physical mixtures to an extent that could hardly be justified by

merely invoking modified dipolar interactions among Fe$_x$O$_y$ domains due to the intervening TiO$_2$ NRs.[1c,14,15,19b]

Various factors can be considered to concur to determine the magnetic response of the HNCs.

The temperature dependence of the ZFC magnetization revealed unusually broad distribution of magnetic anisotropy energy barriers with an atypical size dependence of T_B. In principle, T_B should scale with the Fe$_x$O$_y$ volume, $V_{Fe_xO_y}$, because $T_B \propto K_{eff}*V_{Fe_xO_y}$, where K_{eff} is the effective anisotropy constant. The fact that T_B does not vary smoothly and monotonically, as it does in isolated Fe$_x$O$_y$ NCs,[33,42b,44] indicates that K_{eff} should vary to a different degree. One effect could be correlated to nonmonotonic size-dependence of the relative spinel phase composition that are characterized by different magnetocrystalline anisotropy.[19a,33b,c,42b,44,57] For example, the largest T_B and H_C values recorded for HNCs tipped with ∼15 nm Fe$_x$O$_y$ heads are consistent with the dominance of Fe$_3$O$_4$ phase[33,42b,57] revealed by XANES in this intermediate size regime (Figure 8). Another more relevant effect on the thermal stability of M should arise from existence of a size distribution of interfaces at which different types of chemical bonding, electronic structure, and crystallographic coincidence hold between the b-TiO$_2$ and Fe$_x$O$_y$ lattices. Actually, a relatively large bonding junction (taking a 20−40% fraction of the total Fe$_x$O$_y$ surface) implies interruption of the roughly spherical symmetry of the Fe$_x$O$_y$ domains that would consequently acquire extra shape and surface anisotropy. Interfacial strain can also influence local magnetic ordering to a significant extent.[58] Thus, the existence of b-TiO$_2$/Fe$_x$O$_y$ heterojunctions with variable extension can be expected to affect K_{eff} (which would otherwise be dictated mainly by magnetocrystalline and surface anisotropy) and alter the size-dependence of the energy barrier distribution, otherwise expected for isolated Fe$_x$O$_y$ NCs[1c,d,14,15,19a,54] or for Fe$_x$O$_y$ domains sharing limited contact areas with nonmagnetic materials.[1c,19a]

As for what regards the saturation magnetization, it should be considered that the remarkably lower M_S values characterizing the HNCs, relative to those measured for their isolated Fe$_x$O$_y$ constituents, could hardly be rationalized on the basis of a size-dependence of the relative Fe$_3$O$_4$ to γ-Fe$_2$O$_3$ proportions.[33b−d,42b,44] Therefore, it is reasonable to presume that the ferromagnetic character of Fe$_x$O$_y$ should be strongly depressed in proximity of the interfacial regions, as frequently found for heterostructures based on magnetic and nonmagnetic materials sharing large interfaces[1c,d,15] or undergoing interfacial reactions.[60] Indeed, it is well established that the M_S value in nanostructured spinel

oxides is extremely sensitive to any changes in oxidization state of the spin-disordered surface.[57,58a,60]

Overall, the fact that the detailed structural-compositional features and actual extension of the b-TiO$_2$/Fe$_x$O$_y$ interfaces may broadly vary from one sample to another, also depending on the sizes of the b-TiO$_2$ and Fe$_x$O$_y$ domain components, explains why the individual magnetic parameters share a similar size-dependence despite the absence of any monotonic trend.

4.3. Photocatalytic Properties. In addition to being a magnetically addressable nanocatalyst, our coupled semiconductor heterostructured system represents a complex photochemically active platform for various reasons. First, the HNCs are characterized by a type-I band alignment favorable to carrier migration from the TiO$_2$ to Fe$_x$O$_y$ portion (Scheme 1).[20a,23,25,52a] The heterodimer HNC configuration allows both oxide domains to be exposed to the external environment and participate in interfacial charge carrier transfer. Second, TiO$_2$ is known to be orders of magnitude more photocatalytically active and chemically stable under UV light than spinel Fe$_x$O$_y$, which, in fact, suffers from high probability of electron−hole recombination (facilitated by electron hopping between Fe^{3+} and Fe^{2+} lattice sites).[23,25,45,46] The photoactivity of Fe$_x$O$_y$ under visible illumination is also considered to be irrelevant. Third, the Fe$_x$O$_y$ component itself can exhibit pronounced chemical reactivity, photocathodic corrosion[20a,25,46] and redox reactions in the dark,[20a,21a−e,24,45a,49] depending on the stoichiometry, phase composition, and chemical environment.

Our investigation has been focused on the UV-driven photoactivity of the HNCs in deaerated organic solvents, where reductive-type pathways are enhanced and any inherent Fe$_x$O$_y$-related photocatalytic activity can be safely considered to negligible with respect to that of b-TiO$_2$ under the employed UV irradiation. Because spinel Fe$_x$O$_y$ remains stable against photodissolution, it has been possible to study the inherent effect of an intimate b-TiO$_2$/Fe$_x$O$_y$ heterointerfacing on the ability of TiO$_2$ component to generate and accumulate electrons on the heteronanostructures under continuous irradiation. These properties were assessed by a combination of simple spectrophotometric measurements and electron titration experiments aimed at extracting charges stored on the photocatalysts and using them for dark reductions.

The following major conclusions can be drawn. First, the native $e_{CB}^{TiO_2}$ storing capability of the TiO$_2$ NRs is strongly depressed (down to 5−15%) when photoexcitation is accomplished in the presence of physically interacting or chemically bound Fe$_x$O$_y$ NCs (Figure 10). The lower $e_{CB}^{TiO_2}$ accumulation on the TiO$_2$ NR components can be due to the concurrent effects of Fe$_x$O$_y$ strongly competing with TiO$_2$ for UV photon harvesting and of $e_{CB}^{TiO_2}$ migrating from TiO$_2$ to the Fe$_x$O$_y$ domain due to type-I band alignment (Scheme 1, parts I, III). On the basis of the TiO$_2$/Fe$_x$O$_y$/acceptor energetics (Scheme 1, parts II, IV), these $e_{CB}^{TiO_2}$ are able to reduce both UBA dye and C$_{60}$ acceptors proportionally to their availability (Figure 11).

Second, the UV-irradiated Fe$_x$O$_y$ component appears to undergo topotactic transformation into a Fe$_3$O$_4$-like rich "reduced" form that actually shows dark redox activity analogous to that of half-metallic magnetite.[20a,21a−e,24,45a,49] Such Fe$_3$O$_4$-like domains are indeed capable to contribute to further selective reduction of only C$_{60}$ (cf., Figure 11b,c and e,f) as actually dictated by their lower reduction potential after UV activation, relative to that of reduced TiO$_2$ (cf., $E_{CB}^{Fe_xO_y}$ and $E_{CB}^{TiO_2}$ in Scheme 1, parts II, IV). It is therefore plausible that under our reaction conditions Fe$_x$O$_y$ reduction is achieved as a net result

(57) Schmidbauer, E.; Keller, R. *J. Magn. Magn. Mater.* **1996**, *152*, 99–108.

(58) (a) Salazar-Alvarez, G.; Qin, J.; Sepelac, V.; Bergmann, I.; Vasilakaki, M.; Trohidou, K. N.; Ardisson, J. D.; Macedo, W. A. A.; Mikhaylova, M.; Muhammed, M.; Barò, M. D.; Noguès, J. *J. Am. Chem. Soc.* **2008**, *130*, 13234–13239. (b) Horng, L.; Chern, G.; Chen, M. C.; Kang, P. C.; Lee, D. S. *J. Magn. Magn. Mater.* **2004**, *270*, 389–396. (c) Bollero, A.; Ziese, M.; Höhne, R.; Semmelhack, H. C.; Köhler, V.; Setzer, A.; Esquinazi, P. *J. Magn. Magn. Mater.* **2005**, *285*, 279–289.

(59) (a) Serrano, A.; Fernandez-Pinel, E.; Quesada, A.; Lorite, I.; Plaza, M.; Perez, L.; Jimenez-Villacorta, F.; de la Venta, J.; Martin-Gonzalez, M. S.; Costa-Kramer, J. L.; Fernandez, J. F.; Llopis, J.; Garcia, M. A. *Phys. Rev. B* **2009**, *79*, 144405. (b) Quesada, A.; Garcia, M. A.; Andres, M.; Hernando, A.; Fernandez, J. F.; Caballero, A. C.; Martin-Gonzalez, M. S.; Briones, F. *J. Appl. Phys.* **2006**, *100*, 113909. (c) Garcia, M. A.; Jiménez-Villacorta, F.; Quesada, A.; de la Venta, J.; Carmona, N.; Lorite, I.; Llopis, J.; Fernández, J. F. *J. Appl. Phys.*, in press (available online at http://arxiv.org/abs/0912.3458).

(60) Shendruk, T. N.; Desautels, R. D.; Southern, B. W.; van Lierop, J. *Nanotechnology* **2007**, *18*, 455704.

of TiO$_2$-driven photocatalytic reduction ($e_{CB}^{TiO_2}$ injection is far more dominant over $h_{VB}^{TiO_2}$ injection to Fe$_x$O$_y$ due to efficient $h_{VB}^{TiO_2}$ scavenging by the solvent) rather than of direct Fe$_x$O$_y$ photo-excitation (Scheme 1, parts I, III). Although existence of some $e_{CB}^{Fe_xO_y}$ stored on UV-activated Fe$_x$O$_y$ domains cannot be ruled out, the feasibility of UBA reduction with residual $e_{CB}^{TiO_2}$ trapped in the composite photocatalysts seems to discredit attainment of charge equilibration across the *b*-TiO$_2$–Fe$_x$O$_y$ platforms. In a sense, the Fe$_x$O$_y$ domains combined with photoexcited *b*-TiO$_2$ can be regarded as acting as a redox couple intermediate that serves to indirectly shuttle photogenerated TiO$_2$ electrons to molecular acceptor species with suitable redox potential.

Third, the UV-activated Fe$_x$O$_y$ sections appear to be additionally capable of establishing some peculiar electronic interactions (e.g., formation of charge-transfer complex) with both the unreduced and the reduced acceptor molecules, which lead to distinguishable optical changes. The more pronounced responses observed for the photolyzed HNCs suggest that direct interfacing with TiO$_2$ rendered the Fe$_x$O$_y$ domain more optically sensitive to adhesion of foreign organic species other than the solvent molecules, an effect that may additionally be exploited for sensing purposes.[20,21,24]

5. Summary and Conclusions

We have demonstrated a seeded-growth approach to fabricate topologically controlled magnetic–semiconductor heterodimer HNCs that individually comprise a single spherical Fe$_x$O$_y$ domain epitaxially grown at either one apex or any location along the longitudinal sidewalls of one rod-like *b*-TiO$_2$ section. The synthetic success has been corroborated by a comprehensive compositional-structural investigation disclosing the crystallographic arrangement of the two material lattices and misfit strain distribution across individual heterostructures. On the basis of a wealth of experimental evidence, the different HNC architectures have been discussed within the frame of various mechanistic models offering complementary views of HNC formation. It has been rationalized that topology selection is ultimately achieved by combining suitably structured *b*-TiO$_2$ seeds with Fe$_x$O$_y$-generating pathways that allow seed accessibility to switch from a thermodynamically controlled to kinetically overdriven diffusion-limited deposition regime. It has been proposed that the spatial inhomogeneity of the chemical potential environment around the seeds can play a role in

accentuating their anisotropic reactivity beyond constraints imposed by insurgence of *b*-TiO$_2$/Fe$_x$O$_y$ interfacial strain. These concepts can be useful to deliver additional synthetic criteria for the fabrication of a broad variety of functional heterostructures with a higher level of architectural sophistication and topological precision.

The present *b*-TiO$_2$–Fe$_x$O$_y$ HNCs, which group two valuable representatives of functional nanoscale magnetic and semiconductor materials in a single bifunctional nano-object, can be expected to boost all numerous applications fields related to environmental remediation, catalysis, energy, and biomedicine, which already benefit from titania and iron oxide individually. Our preliminary magnetic and photocatalytic investigations have highlighted that the creation of bonding heterojunctions leads to significantly modified or even unexpected physical-chemical behavior, relative to that offered by *b*-TiO$_2$ and Fe$_x$O$_y$ alone. This allows envisioning that further advances in development of multimaterial heterostructures with ingeniously designed compositional and geometric parameters may offer new sets of properties, not otherwise accessible with the current library of conventional single-component nanostructures, which could open up new opportunities in nanoscience and nanotechnology.

Supporting Information Available: Structure of the dye acceptor used in the titration experiments; additional HRTEM analyses; symmetry of brookite unit cell; modeling and simulations of interface structure; visualization of GPA-derived strain profiles; simplified finite-element calculation of TiO$_2$ elastic response; additional magnetic measurements; additional photocatalytic data; accuracy assessment of GPA strain analysis; and complete ref 10d. This material is available free of charge via the Internet at http://pubs.acs.org.

JA910322A